METAL-SILICATE-SULPHIDE SEGREGATION WITHIN THE YARINGIE HILL METEORITE

By

Harry West

A thesis submitted to Macquarie University
for the degree of Master of Research
Department of Earth and Planetary Sciences

Macquarie Planetary Centre and Macquarie GeoAnalytical (MQGA)

December 2017

Acknowledgements

I would like to sincerely thank my supervisor Bruce Schaefer, who has supported me throughout this entire year and without whom this thesis would not have been possible. Your insight and patience with my many questions has been invaluable and I have learnt a great deal from you.

I would also like to give special thanks to the South Australian Museum who provided a generous sample of the Yaringie Hill meteorite, around which this thesis is based.

I would also like to thank the many others who helped me in this endeavour, in particular, Olivier Alard, whose knowledge of metal and sulphide laser ablation was instrumental to this project, Yi-Jen Lai, who spent many hours helping me during my laser ablation analysis and Tim Murphy for his expertise and assistance with SEM analysis.

I would like to also acknowledge the Macquarie Planetary Research Centre who provided key funding for this project and Macquarie GeoAnalytical for use of their facilities and machine time.

Abstract

The study of the Yaringie Hill meteorite offers a unique opportunity to investigate the early stages of the planetary building cycle, in particular, the mechanisms controlling core formation. This H5 ordinary chondrite features a crosscutting metal vein that has allowed investigation of metal-silicate-sulphide segregation mechanisms on the ordinary chondrite parent body. This study focused on trace element analysis of metals and sulphides using LA-ICP-MS and the establishment of textural relationships through optical and SEM analysis. The vein metal is depleted in HSE relative to matrix metal, and appears to be the result of injection rather than local partial melting. Comparative study against terrestrial and meteoric segregation mechanisms concludes the vein neither formed via shock metamorphism as previously interpreted, or a smelting process. The vein instead appears to be derived from vapour deposition resulting from impact vapourisation. HSE patterns and abundances relative to iron meteorites highlight the vein being transitional toward the IIIAB irons and pallasites, indicating processes like vapour deposition may contribute to final core composition. Further research in this area should focus on building a larger body of research around the mechanism of vapour deposition and its impact on planetary core formation.

Declaration

I certify that the work in this thesis entitled "**metal-silicate-sulphide segregation within the yaringie hill meteorite**"has not previously been submitted for a degree, nor has it been submitted as partial requirement for a degree to any other university or institution other than Macquarie University.

I also verify that this thesis is an original piece of research and has been written by me. Any help and assistance that I have received in my research work and the preparation of the thesis itself have been properly acknowledged.

In addition, I certify that all data, information sources and literature used are indicated in the thesis.

Harry West

Student ID: 43257429

December 20, 2017

Contents

List of Figures

List of Tables

1 — Introduction

While the physical and chemical properties of the differentiated domains of planetary bodies have been researched in great detail, the mechanisms involved in the formation and differentiation of these bodies remain poorly understood. In particular, the mechanisms and time scales involved in the initial segregation of planetesimals and proto-planets into a metallic core and silicate mantle.

Our current constraints on the timing of core formation are based primarily on the Hf-W isotopic system. This chronometer constrains the age of iron meteorites to have formed within 1.5 My of the formation of CAIs, therefore requiring the accretion and differentiation of planetesimals to have been very early and rapid within the solar system. The limitation with using the Hf-W system to constrain core formation is that it relies on complete metal-silicate equilibration, therefore if segregation occurs in partial disequilibrium, the Hf-W system will underestimate the time taken for core formation (Tomkins et al., 2013). Therefore understanding the degree to which each of the metal-silicate segregation mechanisms were involved in core formation is key to us being able to properly constrain the timing of core formation.

1.1 Core Formation Mechanisms

Currently, there have been many proposed core formation mechanisms (Rubie et al., 2007), however, each operate on different time scales and result in diverse chemical signatures for the planetary body. The key mechanisms that appear to have played a role in planetary differentiation are: metal silicate segregation within a magma ocean, percolation driven segregation though solid silicate, impact driven shock metamorphism and smelting of silicate minerals.

1.1.1 Magma Ocean

The most widely accepted mechanism for core formation is metal silicate segregation within a magma ocean (Ricard et al., 2009). In this model, temperatures exceed the silicate solidus, forming a localised or global magma ocean. This allows gravity driven segregation of the denser metal from the more buoyant silicate, where it pools below the molten silicate ocean (Wetherill, 1990). Gravitational instabilities then cause the metal to be transported toward the centre of the planet where it forms the core (Rubie et al., 2003; Stevenson, 1988) (Figure 1.1).

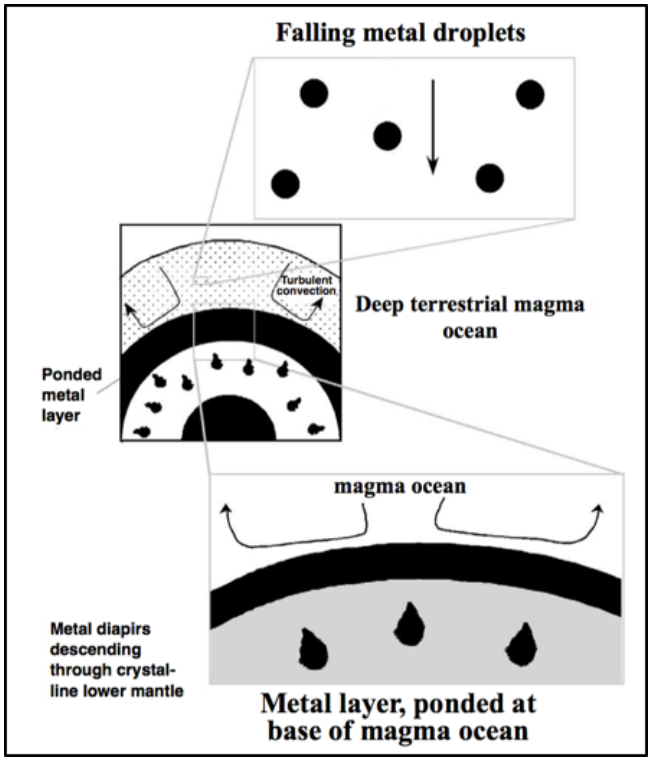

FIGURE 1.1: Model of metal-silicate segregation within a magma ocean. Metal droplets driven by gravity sink through the liquid silicate and pond at the base of the magma ocean. Diapirism and dyking then act as mechanisms to transport the metal through the underlying crystalline mantle to form core. Adapted from Rubie et al. (2003), Figure 1, p.241.

There are three key sources of heat proposed to heat proto-planets and planetesimals above the silicate solidus, and allow the formation of either localised or global magma oceans. These are; energy delivered to the planet through large impactors (Melosh, 1990), radiogenic heating through the decay of ^{26}Al and ^{60}Fe (Urey, 1955; Moskovitz and Gaidos, 2011) and the act of differentiation itself, which lowers the gravitational potential of the body and subsequently releases heat (Rubie et al., 2007).

Radiogenic heating due to the decay of ^{26}Al and ^{60}Fe would have been a key source of heat for planetary bodies, however, due to their short half-lives, their role in planetary differentiation

is limited to the early stages of the solar system (Walter and Trønnes, 2004). They therefore would have been an important source of heat during the accretion of planetesimals, and not the later accretion of proto-planets from planetesimals (Rubie et al., 2007).

Walter and Trønnes (2004) modelled the post accretionary thermal response of planetary bodies with CI chondritic composition and minimum radius 30km, due to the decay of ^{26}Al (Figure 2). The model looks at three initial ^{26}Al/^{27}Al abundance ratios; 5x10^{-5} based on Calcium Aluminium Inclusions (CAIs), 1.5x10^{-5}, and 5x10^{-6} which is based on measurements from carbonaceous chondrites (Kunihiro et al., 2004). Their results (Figure 1.2) show that the effectiveness of heating due to ^{26}Al decay is directly controlled by the initial ^{26}Al/^{27}Al ratios and the timing of accretion. ^{26}Al/^{27}Al ratios above 1x10^{-5} provide enough heating to exceed the Fe-FeS eutectic and begin silicate melting within core timing constraints from the Hf-W system, so long as accretion begins within 1Ma of initial solar system condensation. Ratios less than 1x10^{-5} indicate that for temperatures to reach the silicate melting point and even the Fe-FeS eutectic, another heat source is required.

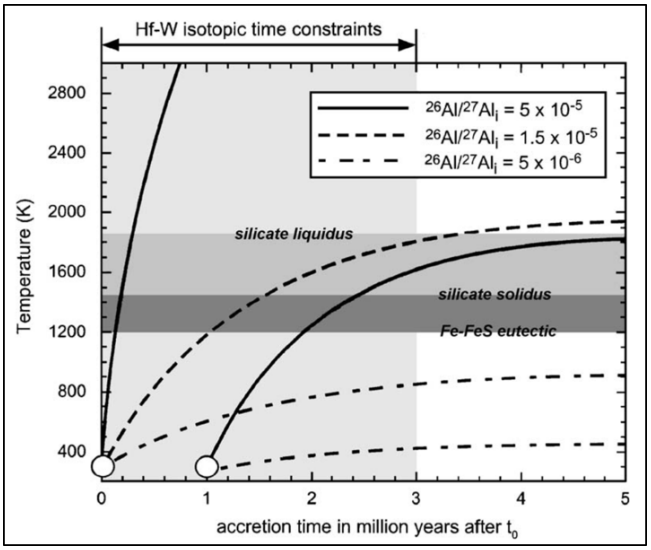

Figure 1.2: Model by Walter and Trønnes (2004) showing the effect of radiogenic heating of a planetary body caused by the decay of ^{26}Al. Model calculated for a body >30km radius with CI Chondritic composition and starting temperature of 255K. Three ^{26}Al/^{27}Al abundance ratios are used to calculate heating trajectories from 0ma and 1ma after initial solar system condensation. Taken from Walter and Trønnes (2004), Figure 1, p.256.

Moskovitz and Gaidos (2011) also modelled the effect of radiogenic heating on a planetesimal due to the decay of ^{26}Al and ^{60}Fe. They used an initial ^{26}Al/^{27}Al ratio of 5x10^{-5} based on CAI concentrations, and an ^{60}Fe/^{58}Fe ratio of 6x10^{-6} based on moddeling by Mishra et al. (2010); Gounelle et al. (2009); Dauphas et al. (2008); Tachibana et al. (2006). Moskovitz and Gaidos (2011)'s model indicates that for planetesimals with a radius greater than 10km that

accreted within 2.7Ma of CAI formation, differentiation is probable.

Heating due to impacts is thought to have been the primary heat source for accreting proto-planets, as their formation time falls mostly outside the critical window for radiogenic heating caused by the decay of ^{26}Al and ^{60}Fe (Rubie et al., 2007). The bulk mass of the terrestrial planets is through to have been derived from the accretion of differentiated planetesimals (Bottke et al., 2006; Baker et al., 2005).

During the accretion of proto-planets, a critical point is reached when their radius becomes >1000km, resulting in enough kinetic energy from incoming planetesimals to initiate local melting (Senshu et al., 2002; Tonks and Melosh, 1992; Davies, 1985). N-body simulations of the later stages of accretion show that impacts increase in energy as an oligarchic accretionary regime takes over, with a few large proto-planets growing quickly, while smaller bodies accrete more slowly (Kokubo and Ida, 1996). This results in increased impacts causing a greater extent of local melting (Samuel, 2012). Eventually giant impacts between bodies occur, delivering extreme amounts of kinetic energy through both the impact and isostatic readjustment post impact that could cause melting on a global scale (Tonks and Melosh, 1992).

Heating due to a reduction in gravitational potential energy is also thought to play a significant role in the differentiation of planetary bodies. An effective lower boundary of a magma ocean is formed where the melt fraction falls below 60% (Solomatov, 2000). This rheological boundary allows segregated metal to pool above the less dense underlying mantle, resulting in a gravitational instability. The redistribution of mass as the denser metal is transported through the underlying mantle toward the core results in the release of gravitational energy (Rubie et al., 2007).

Understanding the physical mechanisms through which metal segregates from silicate in a magma ocean scenario is extremely important as it controls the resulting mantle and core chemistry. The main controls on segregation in a partial or full melt are the size of the metal particles and the viscosity of the silicate. These two factors determine the speed at which segregation can occur and the degree to which metal-silicate equilibration occurs (Rubie et al., 2007). This is extremely important as our current core formation time constraints are based on the Hf-W system which assumes complete equilibration (Tomkins et al., 2013).

As Moskovitz and Gaidos (2011) highlighted, differentiation due to radiogenic heating by of ^{26}Al and ^{60}Fe can differentiate planetesimals within Hf-W time constraints. This means that during the accretion of proto-planets, the impacting planetesimals could have already undergone core-mantle differentiation. During the latter stages of proto-planetary accretion, giant impacts occur which would deliver cores of bodies up to the size of Mars (Tonks and Melosh, 1992). The size of metal bodies segregating through a magma ocean can therefore range over several orders of magnitude, from sub-mm scale (Ichikawa et al., 2010; Rubie et al., 2007) to the already differentiated core of planetesimals and even Mars-sized bodies (Rubie et al., 2007).

Early models of magma ocean segregation showed that metal diapirs would quickly disintegrate into centimetre-millimetre particles within a magma ocean (Ichikawa et al., 2010; Rubie et al., 2003; Stevenson, 1988), resulting in equilibration over a sinking distance of a few tens of metres (Rubie et al., 2003). This idea was challenged by Dahl and Stevenson (2010), whose models of turbulent erosion showed that diapirs >10km in diameter could survive sinking distances of 1000km within a magma ocean without significant loss of volume. This meant that large volumes of metal could be sequestered to the core in disequilibrium with the mantle. Further modelling by Samuel (2012) looked at the stability of iron diapirs sinking through molten silicate over a large range of viscosities. Their results (Figure 1.3) show that the stable limit for iron diapirs have a radius >0.2m for the modelled viscosities. Diapirs greater than their stable limit quickly breakup into smaller bodies within a sinking distance of their initial radius, which then continues until the bodies reach stability. Figure 1.3 shows that for even the most viscous model tested (100 Pa), equilibrium of 99% is reached within a sinking distance of 2km, which is shallow with respect to average magma ocean depths (∼1000km) (Samuel, 2012). This mechanism allows for equilibration of all but the largest diapirs, with the upper limit of a radius greater than the thickness of the magma ocean. Such massive diapirs would be subject to erosion by Kevin-Helmholtz and Rayleigh-Taylor mechanisms as modelled by Dahl and Stevenson (2010), and preserve most of their volume, resulting in sequestration of metal in disequilibrium.

Once the metal has ponded below the magma ocean, gravitational instabilities cause it to be transported to the core via diapirism or dyking (Tomkins et al., 2013). The density contrast between the molten metal and crystalline silicate would cause the formation of metal diapirs whose size and decent rate would be a function on the initial pond thickness and underlying silicate viscosity (Rubie et al., 2007; Karato and Murthy, 1997). Descent rate of the diapirs

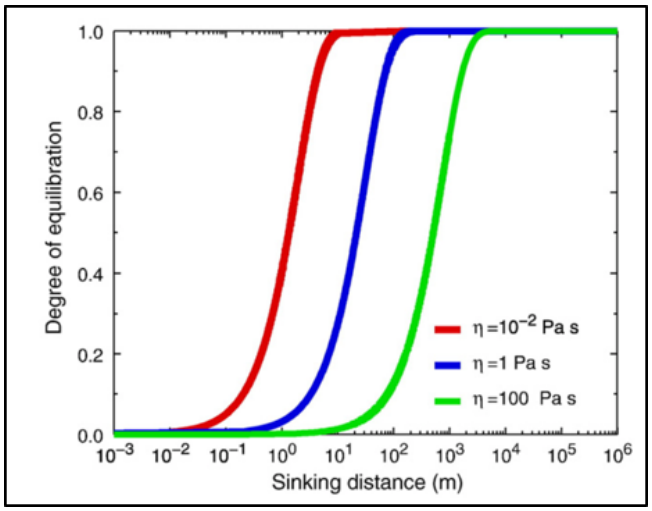

FIGURE 1.3: Results from Samuel (2012) modelling the degree of equilibration for a stable diapir sinking through a magma ocean of various viscosities. Equilibration is achieved quickly even for the most viscous model tested, which is 99% equilibrated sinking only 2km (typical magma ocean depth = ∼1000km). Taken from Samuel (2012), fig. 9, p.113.

would be also further enhanced by gravitational heating, reducing the viscosity of the surrounding silicate (Rubie et al., 2007).

Numerical simulations by Rubin (1995) show that dyking can also be a viable mechanism to transport ponded metal toward the core, requiring a viscosity contrast of greater than 10^{11} - 10^{14}Pa s between molten metal and crystalline silicate. Molten iron has a viscosity of 10^{-2} Pa s, which would allow dike formation to begin through a crystalline silicate with viscosities of around 10^{-9} - 10^{12} Pa s. As the modern day asthenosphere has a viscosity of $\sim 10^{-19}$ Pa s, it is not unreasonable for dike formation to have been a rapid transport process of molten metal to the core (Rubin, 1995). Both diapirism and dyking would allow limited chemical exchange between metal and silicate, and therefore result in disequilibrium.

1.1.2 Percolation

Percolation of metal through solid silicate is thought to have been a viable mechanism for core formation for smaller bodies during the early stages of the solar system (Terasaki et al., 2008). Percolation requires temperatures to reach the Fe-FeS eutectic, allowing molten metal to percolate along the grain boundaries of crystalline silicate, before silicate has reached its melting point. This allows for core formation to begin much earlier than in a magma ocean scenario, and in bodies with concentrations of ^{26}Al and ^{60}Fe too low to reach the silicate solidus through radiogenic heating (Terasaki et al., 2008). High pressure-temperature experiments by Yoshino et al. (2003) have shown that at high dihedral angles (>60°), percolation can occur once the

metallic melt fraction has reached a critical threshold. They estimate this threshold to be as low at 5 vol.% molten iron-sulphur compounds in solid olivine. However as noted by Terasaki et al. (2008), this would still leave at least 5 vol.% molten iron left within the silicate matrix, precluding efficient segregation and core formation. Further work by Walte et al. (2007) also shows that the critical threshold required for dihedral angles >60° could be much higher than 5%, which would result in extremely inefficient core formation.

Modelling by Terasaki et al. (2008) shows that there are several key constraints for percolation to be a viable mechanism of core formation; effective percolation can only occur across olivine grain boundaries where the dihedral angle is >60°, up to 3 GPa and with a high oxygen content. At pressures greater than 3 GPa, the interconnected network shuts down as the dihedral angle becomes greater than 60°. Oxygen solubility is also significantly lowered for S free melts, which makes percolation unlikely. Percolation is therefore only a viable option for small bodies with radii less than 1300 km that are reducing and with high S content, such as the parent bodies for carbonaceous chondrites (Terasaki et al., 2008).

The diffusivity of molten metal in solid silicate is much lower than in liquid silicate, reducing the capacity for equilibration, however due to small silicate grain size and the time scale of percolation, equilibration is possible (Deguen et al., 2011). Numerical modelling by Šrámek et al. (2010); Ricard et al. (2009) show that percolation tends to lead toward coalescence of metal free from silicate, and therefore diapirism, which would reduce surface area to volume and make equilibration insignificant. However, if temperatures reach the silicate solidus before the diapirs have been transported to the core, their instability should lead to their breakup and therefore equilibration as they sink through a magma ocean, as shown by Samuel (2012).

1.1.3 Impact Driven Segregation

Metal-silicate segregation as a result of impact driven shock metamorphism another proposed mechanism for early core formation of planetesimals. Heat generated during impacts cause melting of both metal and some silicate, while pressure gradients drive these melts along fracture pathways. Lower viscosity melts are able to travel much further, allowing Fe and FeS melts to migrate significantly further than any silicate melt generated, allowing the Fe±Ni and FeS melts to propagate into unmelted silicate domains (Tomkins et al., 2013). This process happens very quickly, allowing large accumulations of metal to coalesce in disequilibrium with

the surrounding silicate (Tomkins et al., 2013). As the melt cools and begins to crystallise, the properties of the liquid change from wetting to non-wetting against silicates, causing the expulsion of sulphides into the surrounding silicate material (Tomkins et al., 2013; Rushmer et al., 2005). This results in large accumulations of S depleted, Fe-Ni rich metal in disequilibrium with every impact that generates enough heat to cause melting (Tomkins et al., 2013).

It has been interpreted that non-magmatic iron meteorites are direct evidence for accumulations generated during impact metamorphism. Previous models for the formation of non-magmatic iron meteorites were unable to explain siderophile element signatures seen between melt and chondritic fragments, however impact driven segregation provides a mechanism to explain their trace element compositions (Tomkins et al., 2013). Non-magmatic iron meteorites give us an indication of how large these impact driven accumulations could have been, with the meteorite that formed Meteor Crater in Arizona being estimated to be as large as 3 x 10^8 kg (Tomkins et al., 2013).

Modelling by Tomkins et al. (2013) showed the settling rate of metal globules through peridotite with a melt fraction of 26% allowed for the formation of the core of the asteroid Vesta if the particles were 2m in diameter, which is much smaller than accumulations that form some non-magmatic meteorites. If the melt fraction increases, the viscosity drops by orders of magnitude, allowing particles only 12cm in diameter to form the core of Vesta with a melt fraction of 30% (Tomkins et al., 2013).

Numerical simulations of diapir stability by Samuel (2012) suggest that these diapirs would then breakdown due to instability and equilibrate, however as these accumulations are S depleted, the melting point of pure FeNi is 1425 °C, whereas silicates begin to melt at approximately 1150C (Tomkins et al., 2013). This could result in solid metal accumulations being quickly transported to the core in disequilibrium.

The sequestration of S depleted metal supports the paradox seen in magmatic iron meteorites, thought to be the relict cores of planetesimals, being depleted in S when under equilibrating conditions, such as in the standard magma ocean model, cores should be enriched in FeS potentially up to eutectic proportions (85%) (Tomkins et al., 2013). This would suggest that S depletion in magmatic irons is further evidence of planetesimal core forming under conditions of disequilibrium (Tomkins et al., 2013).

1.1.4 Smelting

Metal silicate segregation may also be achieved by smelting, the reduction of FeO by C, typically seen in Ureilites where olivine is reduced by C as follows the equation $C + MgFeSiO_4 = MgSiO_4 + Fe + CO$ (Warren et al., 2006). While smelting hasn't been proven to be a major contributor to the formation of planetary cores, terrestrial analogues from Disko Island in Greenland show that smelting can result in the formation of native metal from mm sized particles up to several tonnes (Klöck et al., 1986), supporting its potential as a mechanism to aid core formation.

1.2 Core Formation Conclusions

It seems very likely that core formation did not result from a single mechanism scenario as is often modelled, rather it was driven by a variety of mechanisms, each operating throughout different periods during accretion.

Impact driven segregation would have been one of the earliest operating mechanisms, allowing the formation of large accumulations of FeNi metal before the body has had time to reach the silicate solidus (Tomkins et al., 2013). If a planetesimal had formed after the peak period for heating via radioactive decay, impact driven segregation would have formed larger accumulations of metal that could settle through partially molten silicate at low melt fractions of 26-30% (Tomkins et al., 2013).

Radiogenic heating due to the decay of ^{26}Al and ^{60}Fe provides a viable mechanism for heating of planetesimals above the silicate solidus and allowing the formation of either localised or global magma oceans where gravity driven segregation of metal and silicate would occur (Moskovitz and Gaidos, 2011; Walter and Trønnes, 2004).

Percolation may have also played a role in the formation of cores in planetesimals, however due to the limitations discussed with percolation, its usefulness may have been limited to smaller bodies with high S content (Terasaki et al., 2008). Smelting could have also played a minor role in the differentiation of bodies with enough C to reduce FeO in olivine crystals.

A combination of both metal silicate differentiation within either localised or a global magma

ocean, and the quick sequestration of large accumulations of metal due to impact driven segregation appears to be a likely scenario for core formation in planetesimals, however the degree of equilibration that occurred within these bodies is still poorly constrained. Impact metamorphism would have resulted in the settling of metal in disequilibrium, however, once the viscosity of peridotite had been lowered due to increased heating, the stability of the metal diapirs would have been greatly reduced, allowing equilibration under a magma ocean scenario (Samuel, 2012). Complete equilibration for planetesimals seems very unlikely in all bodies except those that accreted rapidly with very high concentrations of ^{26}Al and ^{60}Fe, allowing the swift formation of a global magma ocean. This would mean that our current timing constraints based on Hf-W chronometry from iron meteorites system would underestimate core formation time (Tomkins et al., 2013).

Core formation in accreting proto-planets would have been very similar to planetesimals. Impact driven segregation would have been ongoing with every impact great enough to generate partial melting of metal and silicate (Tomkins et al., 2013). Heating of the proto-planet to form a localised or global magma ocean would have been primarily driven by the energy delivered by impacts as well as heating via the reduction of gravitational potential (Rubie et al., 2007). Sinking diapirs would be equilibrated in a magma ocean, with the exception of those that had a radius of equal to or greater than the depth of the magma ocean, as may be the case for the cores of impacting proto-planets and planetesimals. In this case, they would be partially eroded by Kevin-Helmholtz and Rayleigh-Taylor mechanisms, however would retain most of their volume and be transported to the core in disequilibrium (Dahl and Stevenson, 2010). Again, while some equilibration would have occurred, it seems very unlikely that an accreting planet would achieve full equilibration. This would mean that our current estimations of core formation time based on the Hf-W system underestimate the time taken for core formation (Tomkins et al., 2013).

2 — Aims and Objectives

The study of meteorites provides snapshots of all stages of planetary formation. Significantly, they offer insights into the most difficult to access portions of the planetary building cycle, notably core formation and stabilisation. Chondrites are thought to represent some of the earliest undifferentiated solar system material, while iron meteorites represent the cores of early planetesimals that underwent metal-silicate segregation before their subsequent destruction (Rubie et al., 2007). Pallasites are widely accepted to be remnants of the later stages of metal silicate segregation along the core-mantle boundary of early planetesimals (Mullane et al., 2004). Other meteorites have been interpreted to represent the process of various differentiation mechanisms such as smelting forming Ureilites (Warren et al., 2006) and shock metamorphism forming the non-magmatic iron meteorites (Tomkins et al., 2013).

Understanding the processes behind core formation is particularly important as the formation of a core is vital to the evolution of life, as the magnetic field it generates helps protect the earth from solar winds. Core formation is also vital to large scale volcanic activity on planets as the interaction at the core mantle boundary is thought to be responsible for plume magmatism (Campbell and Humayun, 2005).

The Yaringie Hill meteorite is an H5 ordinary chondrite that was found in 2006 in the Gawler Ranges, South Australia (Tappert et al., 2009). It was chosen for this study as it features a thin (0.5mm) metal vein that cross-cuts the entire meteorite (Figure 4.1). The vein has been interpreted to be the result of shock metamorphism (Tappert et al., 2009) and allows us to study the early stages of metal-silicate-sulphide segregation within chondritic material.

In order to better elucidate the chemical and physical controls associated with core formation, this project aims to investigate trace element segregation between metal and sulphides in the matrix and the vein of this meteorite. Ordinary chondrites, although the most common type

of meteorite, are relatively poorly investigated in terms of metal-silicate-sulphide partitioning, with many studies focusing instead on the more chemically reducing carbonaceous chondrites (Ziegler et al., 2010; Jurewicz et al., 1993). Yaringie Hill therefore represents a unique opportunity to empirically constrain the processes involved in metal-silicate-sulphide segregation within undifferentiated ordinary chondrite material.

This project incorporates an optical and SEM (Scanning Electron Microscopy) campaign to establish the textural relationships between the vein and the host material in the Yaringie Hill meteorite. This offers the basis to test whether the vein material is indeed derived from in-situ melting, or potentially derived from elsewhere in the parent body. This then provides the basis for a LA-ICPMS (Laser Ablation - Inductively Coupled Plasma Mass Spectrometry) campaign using transition metals and PGEs (Platinum Group Elements) to evaluate the likely provenance of the metal.

Based on the presence of a cross-cutting metal vein through the ordinary chondrite matrix of the Yaringie Hill meteorite, an opportunity exists to ascertain:

1. Whether the textural relationships between the vein and the matrix metals suggest localised melting and extraction of metal, or derivation from elsewhere in the parent body.

2. LA-ICPMS analysis of trace metals and PGEs in metals and sulphides within the matrix and vein allows quantification of fractionation of metals within the OC (Ordinary Chondrite) parent body.

3. Testing whether shock melting of matrix metal and local extraction into the vein is a viable mechanism for Yaringie Hill. This model would predict injection of the metal into the chondritic matrix and subsequent expulsion of sulphides from the vein into the fracture networks of the matrix on crystallisation (Tomkins et al., 2013).

4. An alternative process involving the trace element and PGE behaviour during reduction from a silicate melt is tested empirically through analysis of a terrestrial analogue from Disko Island, Greenland.

5. The relative fractionations and partition coefficients in each of the relevant scenarios are then calculated and compared with literature values in order to derive a preferred model for metal melting and extraction on the ordinary chondrite parent body. This allows comparison with other metals within early solar system bodies and hence inform the

discussion surrounding the ultimate source of metals that are available to participate in core formation on planetesimals.

3 — Methodology

In order to investigate the mechanism of metal-silicate-sulphide segregation within the Yaringie Hill meteorite and Disko Island native iron, an analytical campaign was planned to obtain high quality quantitative data for major, minor and trace elements as well to observe and image key textural features that could give us insight into the physical and chemical mechanisms controlling the formation of the vein.

3.1 Samples

In total 10 samples of the Yaringie Hill meteorite were prepared and one Disko Island sample. The meteorite slab was cut into 5 blocks, each prepared into 30μm polished thin sections on glass slides for Scanning Electron Microscopy (SEM) analysis. The single Disko Island sample was prepared into a polished block. An Edwards Auto306 vacuum coater was then used to carbon coat Yaringie samples YH1 to YH5 and the Disko Island sample for SEM analysis. The other halves of the 5 meteorite blocks were then prepared into 100μm polished thick sections on glass slides for analysis by Laser Ablation - Inductively Coupled Plasma - Mass Spectrometry (LA-ICP-MS) (Samples YHT1-YHT5). Due to budget restraints, only three of the five thick sections were able to be analysed, so the best three were selected using reflected microscopy. The Disko Island polished block was also analysed using LA-ICP-MS. All thin and thick sections were analysed by transmitted and reflected microscopy and the Disko sample was analysed under reflected microscopy. All samples were stored in a sealed container to ensure they remained free from any contamination. Table 3.1 summarises the samples and analytical techniques.

Table 3.1: Summary of samples and analytical techniques

Sample	Type	Optical	SEM	LA-ICP-MS
YH1	30μm Thin Section	✓	✓	
YH2	30μm Thin Section	✓	✓	
YH3	30μm Thin Section	✓	✓	
YH4	30μm Thin Section	✓	✓	
YH5	30μm Thin Section	✓	✓	
YHT1	100μm Thick Section	✓		✓
YHT2	100μm Thick Section	✓		
YHT3	100μm Thick Section	✓		
YHT4	100μm Thick Section	✓		✓
YHT5	100μm Thick Section	✓		✓
Disko Island	Polished Block	✓	✓	✓

3.2 Optical Microscopy

All samples were first examined by both transmitted and reflected microscopy using a Nikon Eclipse 50iPOL microscope equipped with a Nikon DS-U2/L2 USB Camera. The microscope was setup with a PRIOR motorised stage, connected to a computer running PRIOR's software. This allowed large areas of the thin and thick sections to be photographed under transmitted and reflected light, before being stitched together into a single large image in order to plan analysis areas and as a reference map during SEM and LA-ICP-MS analysis.

3.3 Scanning Electron Microscopy

Zeiss Evo MA 15 scanning electron microscope with an Oxford Instruments X-Max 20mm^2 silicon drift detector with an energy dispersive (EDS) detector was used to obtain quantitative major and minor element data from samples YH1-YH5 and the Disko Island sample. Secondary electron (SE) and backscatter electron (BSE) images were also captured using the SEM. Data was able to be viewed in real time using the Oxford Aztec EDS analysis software suite. Data was exported after analysis and processed on a separate computer using the Oxford Aztec EDS analysis software suite.

The scanning electron microscope was run in point analysis mode to collect major and minor element quantitative data for all samples, and element maps were run on the Yaringie samples to distinguish various mineral phases and to look for any partitioning of major elements along the vein. Backscatter and secondary electron images also allowed us to examine

textural features of the vein system in much greater detail than was possible using reflected light microscopy. The quantitative data obtained during analysis of the Yaringie Hill and Disko Island metals and sulphides was also used as an internal standard during LA-ICP-MS.

The Zeiss Evo MA 15 scanning electron microscope was operated with an accelerating voltage of 15kV, beam current of 20nA and a working distance of 12mm. Target input counts were 60,000 and target dead time was 40%. A copper grid was analysed every hour during analysis to perform an energy calibration to increase accuracy and reliability of the data. Analysis are calibrated against standards from the Oxford Aztec EDS analysis software.

Scanning electron microscopy was chosen as our method of collecting major and minor element data over other analytical techniques such as X-Ray Fluorescence (XRF) and electron microprobe analysis (EMPA) as it allowed us to take in situ analysis of our sample which cannot be achieved with XRF, and at a more cost effective price than EMPA, allowing us to better direct a larger portion of our budget to trace element analysis using LA-ICP-MS.

3.4 Laser Ablation - Inductively Coupled Plasma - Mass Spectrometry

Trace element data was obtained at Macquarie Univerity GeoAnalytical (MQGA) Laboratories using LA-ICP-MS. Laser Ablation ICPMS was selected in preference to other solution ICPMS methods as it allows in-situ analysis of both metal and sulphide grains in the vein and matrix, giving us spatially resolved data at similar detection levels, opposed to a bulk composition for the samples.

Laser abalation was conducted using a Photon Machines Excite Excimer 193 nm laser ablation microprobe coupled to an Agilent 7700cx quadrupole ICPMS. Argon was used as a carrier gas of the analyte into the ICP torch.

Counting times for the Yaringie Hill samples were 120s of background measuring a gas blank before 60s of ablation time, followed by 60s of washout time. All standards were analysed with a spot size of 65μm, kamacite grains were analysed with spot sized of 65-85μm and troilite grains were measured with a spot size of 110μm. Variation in spot size was due to a need to

balance low element concentrations and spacial resolution. All Analysis were carried out with a pulse rate of 7Hz, burst count of 400 and laser energy of 75%.

Counting times for the Disko Island samples were 120s of background measuring a gas blank before 60s of ablation time, followed by 60s of washout time. All analysis were carried out using a spot size of 65μm, pulse rate of 10Hz, burst count of 600 and laser energy of 75%.

Analysis of each sample was undertaken in runs of 10, bracketed by analysis of each standard, with double measurements of each standard at the beginning and end of the analysis session.

Normalisation to both an internal and external standard is necessary for LA-ICP-MS data as it corrects for any variation in ablation yield and instrument drift over the course of analysis (Longerich et al., 1996; Longerich, 1996). The internal standard chosen must be a major or minor element that is present in both the analyte and external standard. Ni was chosen for metals analysed and S for sulphides. Both internal standards were determined for the Yaringie Hill and Disko Island samples using quantitative data obtained during SEM analysis.

The external standards chosen were PGE_A, N661, N1262 and JK37 as they allowed analysis of all selected isotopes. Isotopes measured were; Si^{29}, P^{31}, S^{34}, V^{51}, Cr^{52}, Mn^{55}, Fe^{57}, Co^{59}, Ni^{60}, Ni^{62}, Cu^{63}, As^{75}, Se^{77}, Nb^{93}, Mo^{95}, Ru^{99}, Ru^{101}, Rh^{103}, Pd^{105}, Pd^{106}, Ag^{107}, Pd^{108}, Sn^{118}, Sb^{121}, Te^{125}, Te^{126}, Os^{189}, Os^{192}, Ir^{193}, Pt^{194}, Pt^{195}, Au^{197}, Pb^{208}, with counting times for each chosen based on expected concentrations.

The standards chosen for each isotope are displayed in Table 3.2. The average value and number of analysis is shown for each isotope and confidence is reported as $\pm 1\sigma$ and Relative Standard Deviation % (RSD%). The reference value is also displayed with $\pm 1\sigma$ uncertainty. The long term reproducibility for the analysis can be calculated from the 1σ uncertainty of the average of the standards used.

TABLE 3.2: Standards analysed for each isotope

Isotope	Standard	n	Avg (ppm)	$\pm 1\sigma$ (ppm)	RSD%	Reference Value (ppm)	$\pm 1\sigma$ (ppm)
Si29	N661	5	2621.37	973.53	37.14	2330.0	10
P31	N661	5	150.10	15.55	10.36	150.0	10
S34	N661	2	169.24	34.95	20.65	150.0	10
V51	JK37	6	724.66	65.72	9.07	750.0	40
Cr52	N1262	6	3315.79	532.45	16.06	3000.0	100
Mn55	N661	6	6505.75	294.64	4.53	6600.0	100
Fe57				Wt% based off SEM analysis			
Co59	N661	6	314.17	12.53	3.99	320.0	10
Ni60							
Ni62				Used as an internal standard			
Cu63	N1262	6	5051.81	211.67	4.19	5100.0	100
As75	PGE_A	10	131.56	3.04	2.31	131.0	13.1
Se77	PGE_A	10	226.51	17.78	7.85	227.0	22.7
Nb93	JK37	6	12.96	3.90	30.07	12.0	2
Mo95	JK37	6	35259.34	12737.35	36.12	35500.0	350
Ru99	PGE_A	10	207.17	15.03	7.26	203.0	20.3
Ru101	PGE_A	10	223.13	14.46	6.48	203.0	20.3
Rh103	PGE_A	10	223.13	14.46	6.48	220.0	22
Pd105	PGE_A	10	268.41	28.44	10.60	271.0	27.1
Pd106	PGE_A	10	269.04	27.55	10.24	271.0	27.1
Ag107	PGE_A	10	225.83	14.95	6.62	229.0	22.9
Pd108	PGE_A	10	269.26	28.70	10.66	271.0	27.1
Sn118	N1262	6	158.11	8.15	5.16	160.0	20
Sb121	N1262	6	118.51	6.78	5.72	120.0	6.2
Te125	PGE_A	10	201.28	9.49	4.71	214.0	21.4
Te126	PGE_A	10	200.67	10.86	5.41	214.0	21.4
Os189	PGE_A	10	74.64	10.28	13.77	72.7	4.8
Os192	PGE_A	10	75.32	10.67	14.17	72.7	4.8
Ir193	PGE_A	10	126.16	13.32	10.56	208.0	20.8
Pt194	PGE_A	10	192.79	15.37	7.97	204.0	20.4
Pt195	PGE_A	10	192.22	14.99	7.80	204.0	20.4
Au197	PGE_A	10	211.78	9.84	4.65	212.0	21.2
Pb208	PGE_A	10	28.86	3.57	12.37	29.0	2.9

Standards N661 and N1262 are standard reference materials that are certified by the National Institute of Standards and Technology. Standard JK37 is a Sweedish steel certified reference material by the Swedish Institute for Metals Research. Standard PGE_A is an in house standard that has been well characterised by previous publications (Gilbert et al., 2013; Alard et al., 2000).

4 — Sample Descriptions

The Yaringie Hill meteorite (Figure 4.1) is a weakly shocked, H5 ordinary chondrite that was found in 2006 within the Gawler Ranges, South Australia (Tappert et al., 2009). The chondrite has been recrystallised and is covered by a thin brown fusion crust (Tappert et al., 2009). An interesting feature of the meteorite is a thin (0.5mm) metal vein composed of the FeNi alloy kamacite.

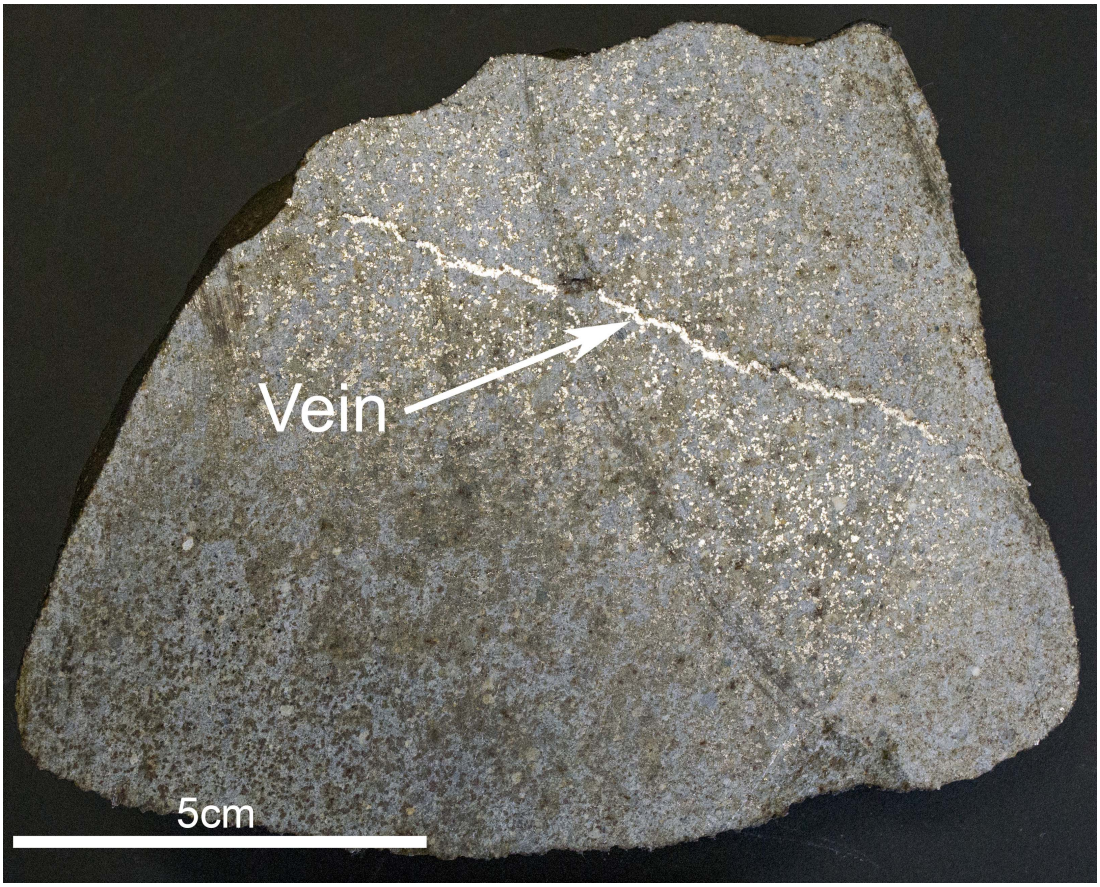

FIGURE 4.1: The Yaringie Hill meteorite with cross-cutting kamacite vein.

The main minerals forming the meteorite are olivine, orthopyroxene and phases of iron-nickel alloys (Figure 4.2). Olivine and orthopyroxene occur both within the matrix as distinct crystals and as inclusions within chondrules. They both exhibit undulatory extinction which has been interpreted by Tappert et al. (2009) to be an indicator of shock metamorphism, along

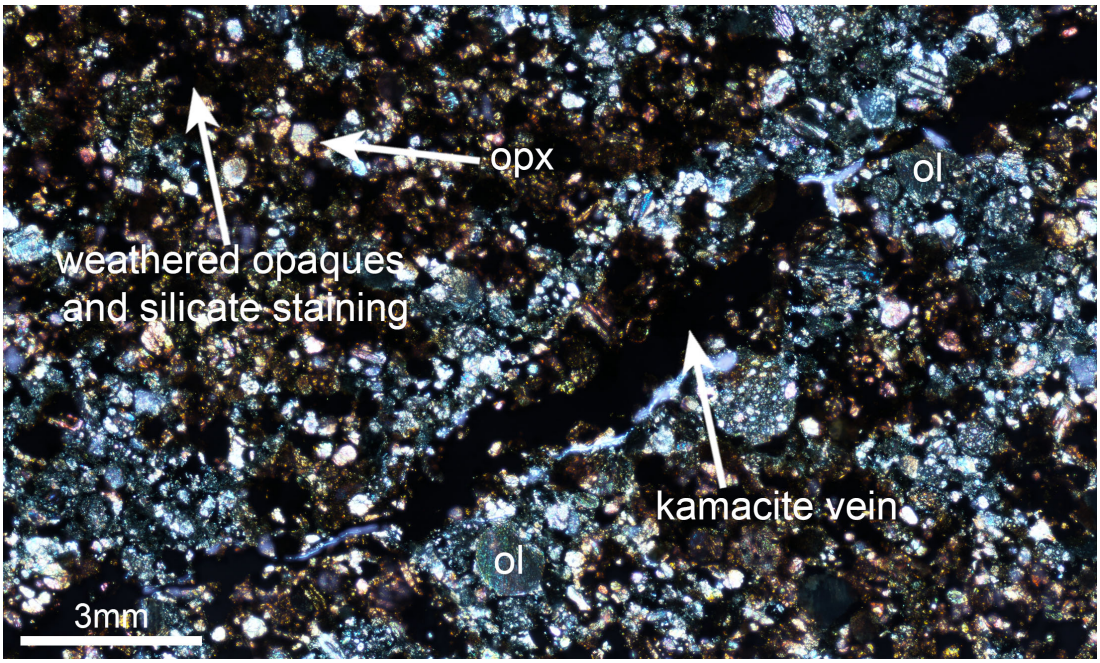

FIGURE 4.2: Photomicrograph (crossed polars) of the Yaringie Hill meteorite vein and surrounding silicate matrix. Large orange areas are due to oxide weathering of opaque minerals, staining the surrounding silicates.

with planar fractures in olivine crystals and the presence of the kamacite vein. Under the classification scheme by Stöffler et al. (1991), Tappert et al. (2009) has classified the Yaringie Hill meteorites as being weakly shocked to stage S3. Kamacite forms the vein and is the main FeNi alloy within the matrix (Figure 4.3). Other alloys include taenite and tetra-taenite. Tappert et al. (2009) has classified the meteorite as experiencing weathering stage W1 as defined by Wlotzka (1993), and weathering of FeNi alloys and troilite grains within the matrix and vein has caused oxide staining of some of the surrounding silicates (Figure 4.2). Troilite is an Fe sulphide that can be seen within the vein as rounded grains, indicating it was an immiscible melt phase within the vein as can be seen in Figures 4.3 and 6.8. Troilite can also be seen as anhedral grains within the matrix.

The Disko Island sample is composed of aphanitic basalt that hosts μm to mm sized native iron grains and sulphides. The iron was formed from a smelting reaction as a basaltic lava flowed over carbonaceous shales and Tertiary coals on Disko Island, Greenland (Klöck et al., 1986). This allowed silicates within the basalt to be reduced by carbon from the coal, resulting in the production of native iron. The Disko Island deposit of native iron represents the largest of only a few such deposits in the world, producing iron that ranges from μm sized grains to blocks that weigh several tonnes (Klöck et al., 1986).

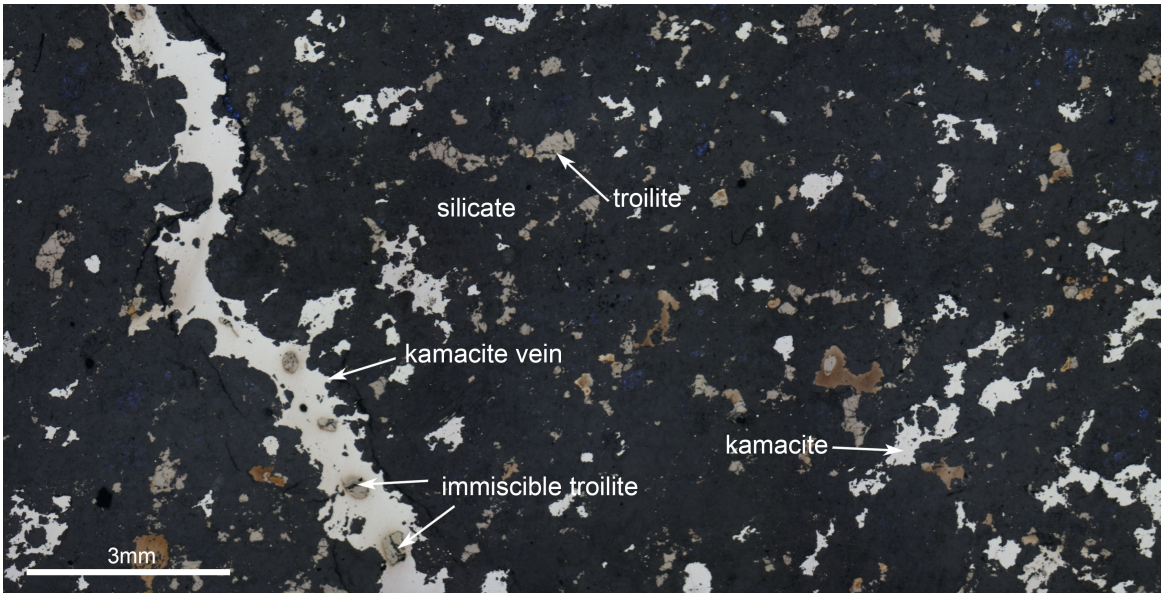

FIGURE 4.3: Photomicrograph (reflected light) of the Yaringie Hill meteorite.

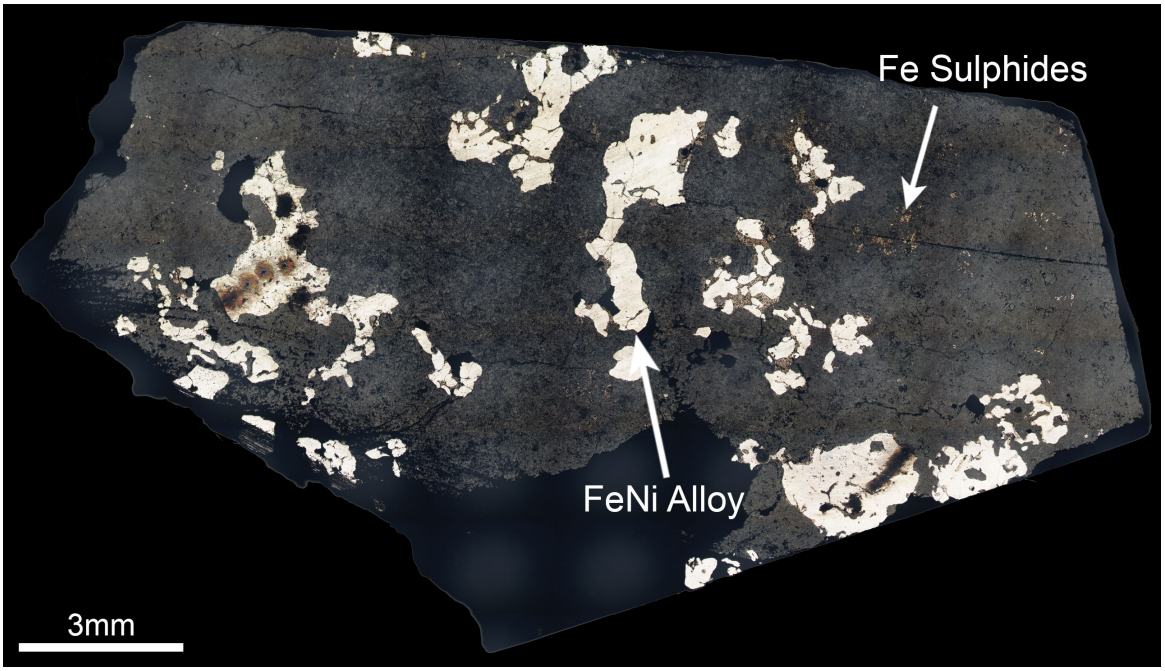

FIGURE 4.4: Photomicrograph (reflected light) of the Disko Island sample. Metal and sulphides are surrounded by aphanitic basalt.

5 — Results

5.0.1 Major and Minor Element Results

Scanning electron microscopy has allowed us to image key textural features and obtain quantitative major and minor element data of the Yaringie Hill meteorite and Disko Island sample. Element maps and backscatter photos have been used to observe the textural relationships, while point analysis has enabled us to quantify major elements within metals and sulphides.

An Fe Ni S element map of a section of the vein undulating around a chondrule of the matrix is shown in Figure 5.1. The element map allows us to highlight only the elements of interest, better displaying the data to the phases we want to investigate. We can see that there are three key FeNi and FeS phases within the Yaringie Hill meteorite; kamacite (red), taenite (blue) and troilite (green). Kamacite can be seen forming the vein and as anhedral grains within the matrix ranging in size from μm to mm. Kamacite can also be seen forming apophyses extending from the vein into the matrix. Taenite is seen along the edges of the vein and occurring in small anhedral grains within the matrix either by itself or along the edges of kamacite or troilite grains. Troilite can be seen as small anhedral grains within the matrix, and also as rounded grains within the vein indicating that is was an immiscible melt phase within the vein (Figures 4.3 and 6.8). The inset in Figure 5.1 shows the same image, captured in backscatter to better show the vein undulating around the chondrule.

Fe v Ni (Wt%) for the Yaringie matrix and vein Kamacite plotted against the Disko Island iron is displayed in Figure 5.2. We can clearly see that the Yaringie kamacite from both vein and matrix plot very closely together, with very little variation in both Fe and Ni. The Disko Island iron however displays a range in iron concentration, with little variation in Ni.

Fe v S (Wt%) for the Yaringie troilite from the matrix and the vein plotted against the

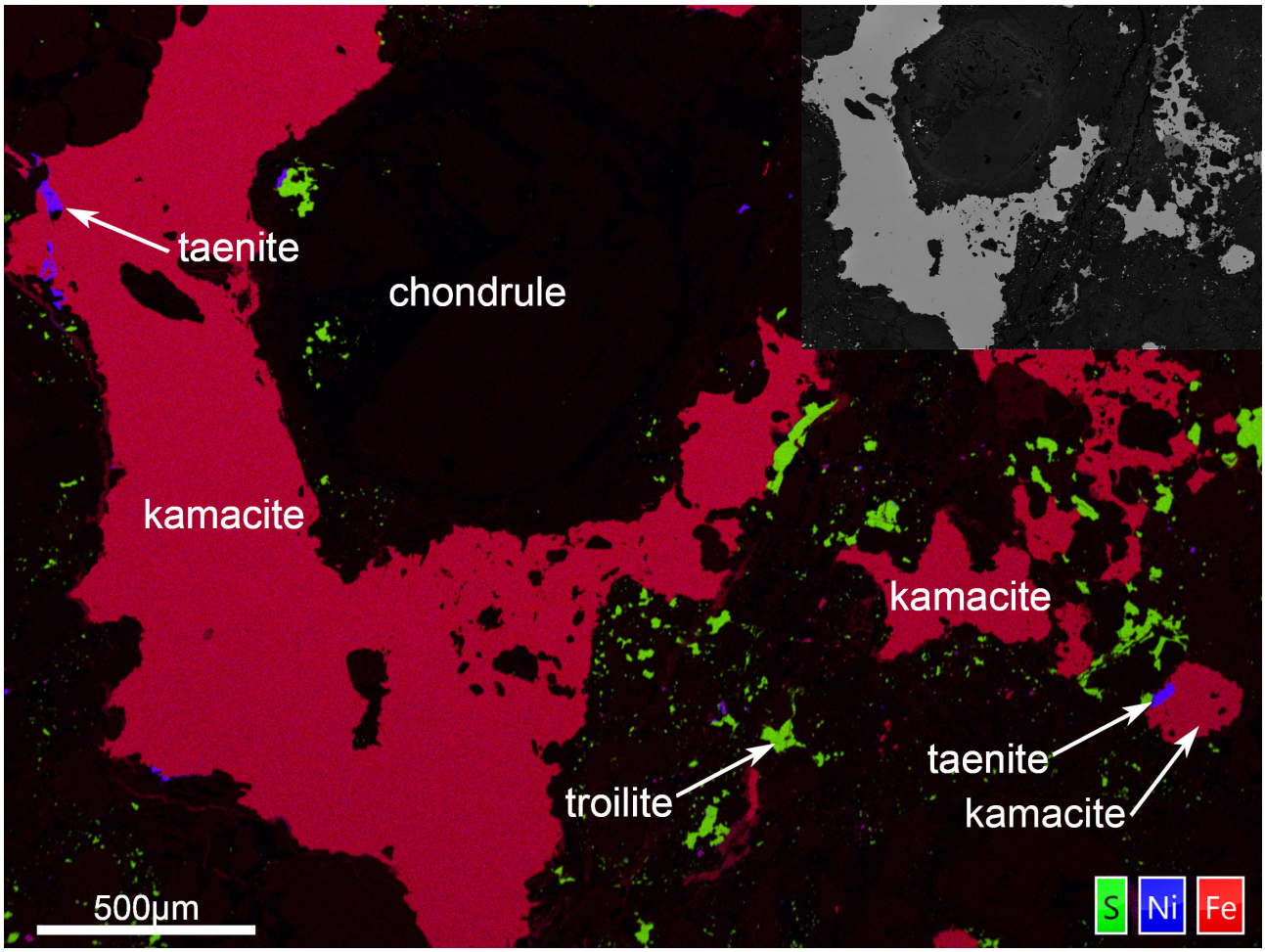

FIGURE 5.1: Fe Ni S element map showing the Yaringie Hill meteorite vein undulating around a chondrule of the matrix. Inset shows the same image in backscatter, better highlighting the undulation around the chondrule.

Disko Island troilite is illustrated in Figure 5.3. We can see that there is a small amount of variation in the troilite of the Yaringie Hill meteorite, with two phases within the matrix; a lower Fe and higher S phase that plots the same as the vein, and a slightly higher Fe and lower S phase. The Disko Island troilite experiences much more variation with a range of both Fe and S concentrations.

Fe Ni and S average values in Wt% for the metals and sulphides of Yaringie Hill meteorite are displayed in Table 5.1. Detection limits have been reported as ranges in wt% σ for each element, as detection limits from EDS will vary with each individual analysis.

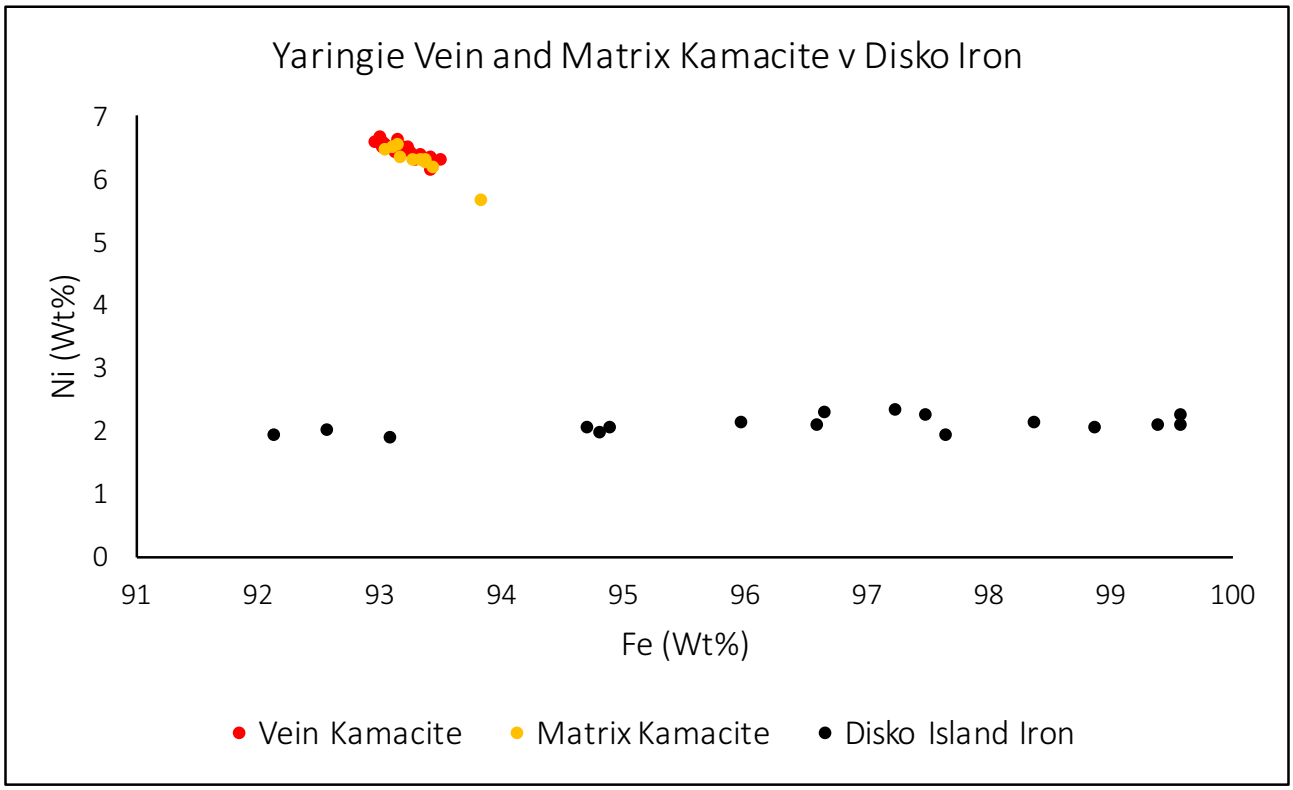

FIGURE 5.2: Fe v Ni (Wt%) for the Yaringie vein and matrix kamacite and Disko Island iron.

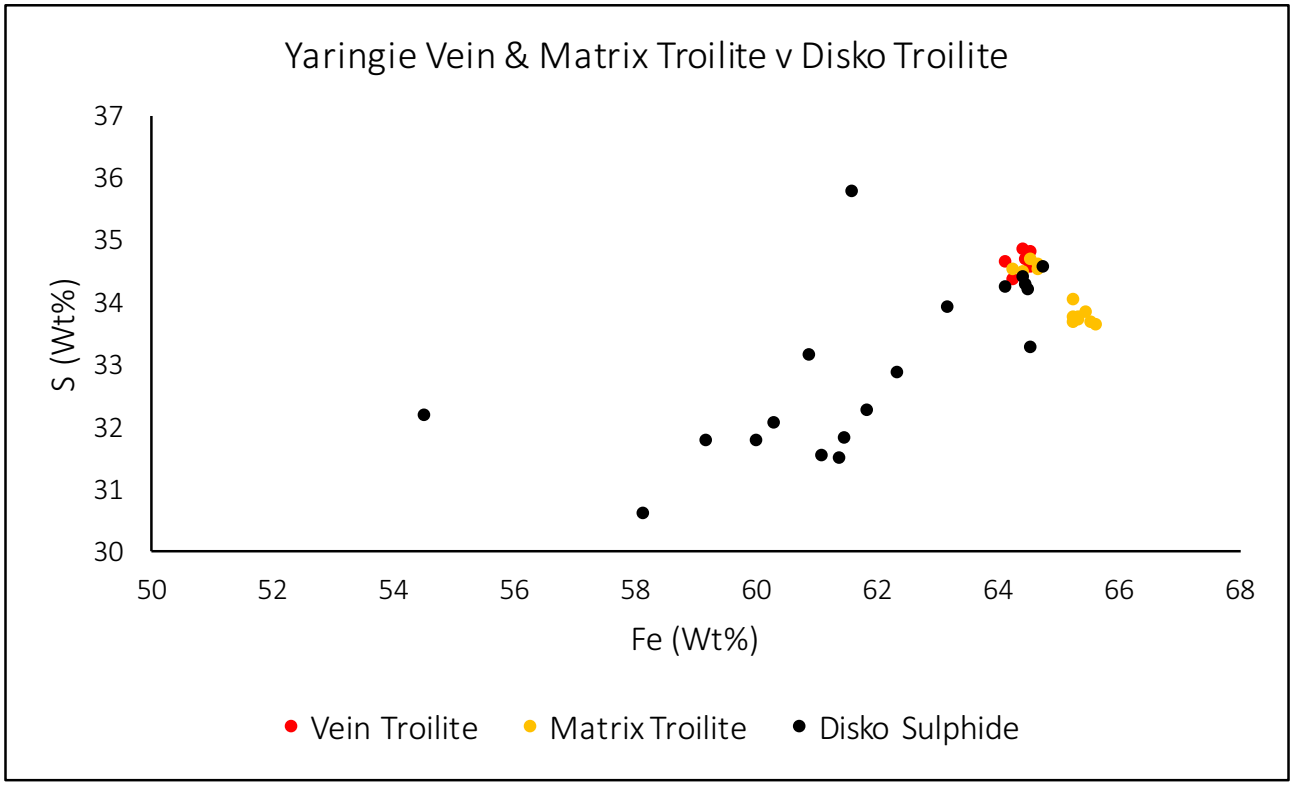

FIGURE 5.3: Fe v S (Wt%) for the Yaringie vein and matrix troilite and Disko Island troilite.

TABLE 5.1: Representative compositions for metals and sulphides of the Yaringie Hill meteorite and Disko Island sample

Mineral	No. of analysis	Fe	Ni	S
Vein Kamacite	22	93.18	6.45	b.d.l.
Matrix Kamacite	10	93.32	6.28	b.d.l.
Vein Troilite	7	64.44	b.d.l.	34.60
Matrix Troilite	13	65.05	b.d.l.	34.04
Matrix Taenite	1	80.82	18.94	b.d.l.
Matrix Tetra-taenite	3	49.84	49.81	b.d.l.
Disko Island Iron	10	96.45	2.08	b.d.l.
Disko Island Troilite	10	61.72	b.d.l.	32.92

Detection limits are based on counts and vary for each individual analysis. Detection limits for Ni and S are; Ni (0.08-0.10), S(0.09-0.10), reported in wt% σ.

5.0.2 Trace Element Results

LA-ICP-MS has allowed us to quantify trace element concentrations for metals and sulphides in both the Yaringie Hill meteorite and Disko Island sample. Presented here are average values for each metal and sulphide, individual analysis points can be found in the Appendix within Tables 1 to 7.

Vein kamacite and matrix kamacite average results of the Yaringie hill meteorite, normalised to C1 chondrite from McDonough and Sun (1995) are displayed within Figure 5.4. The raw data for this graph can be seen in Table 5.2. Overall, the two metals follow very similar patterns, with the vein kamacite being slightly more depleted in all elements with the exception of S, Nb, Ag and Sn. The vein is depleted in the highly siderophile elements relative to the matrix.

The average analysis of troilite of the vein and the matrix of the Yaringie Hill meteorite are highlighted in Figure 5.5. The raw data for this graph can be seen in Table 5.3. Again the troilite patterns follow very similar trends to the kamacite, with the vein being overall more depleted than the matrix, with the strongest relative depletion seen within the highly siderophile elements.

Figure 5.6 displays the calculated partition coefficients in lithophile, chalcophile and siderophile element order. The partition coefficient for sulphide/metal for the vein is represented by $kD_{vs/vm}$ and the matrix $kD_{ms/mm}$. The sulphide/metal partition coefficients for the vein and matrix highlight the lithophile and chalcophile elements having a strong affinity for the sulphide phase,

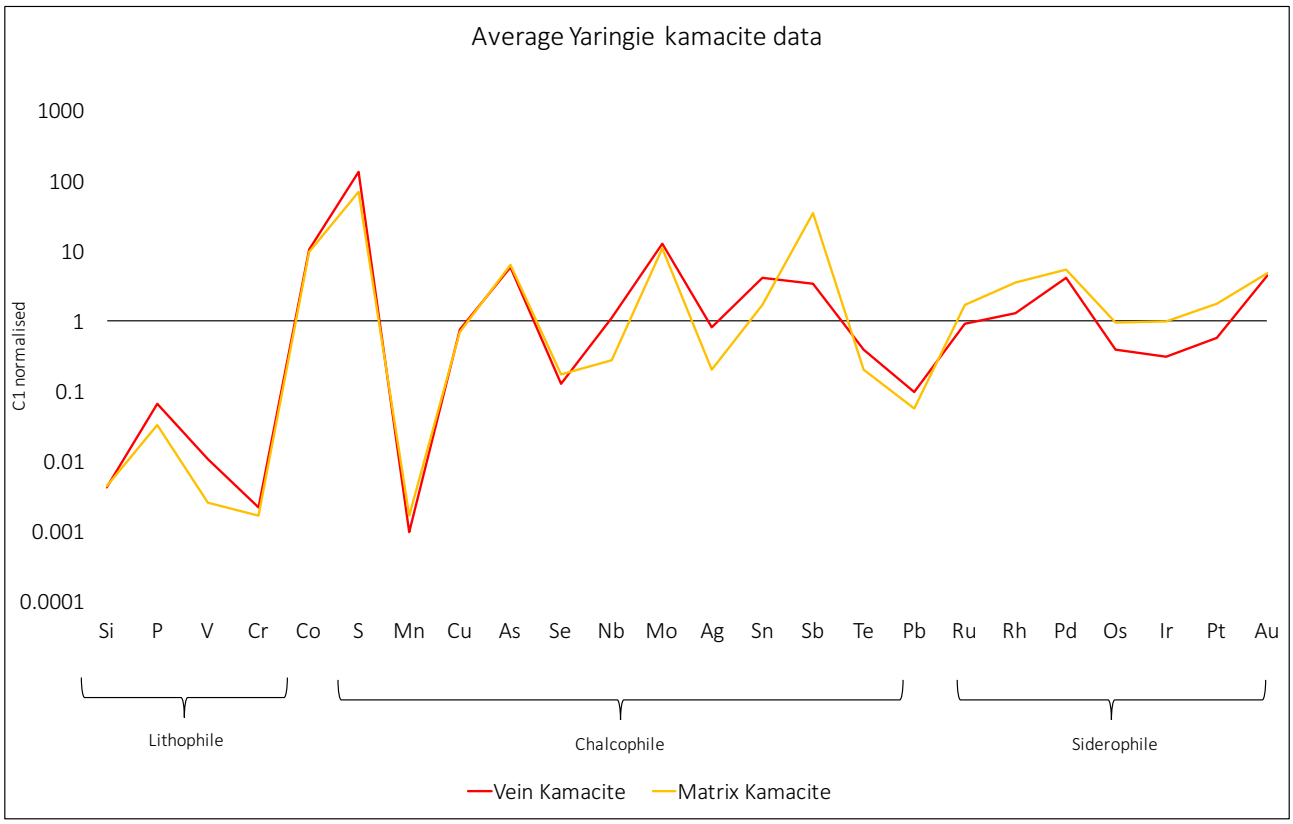

FIGURE 5.4: Average kamacite composition for the lithophile, chalcophile and siderophile trace elements of the vein and matrix.

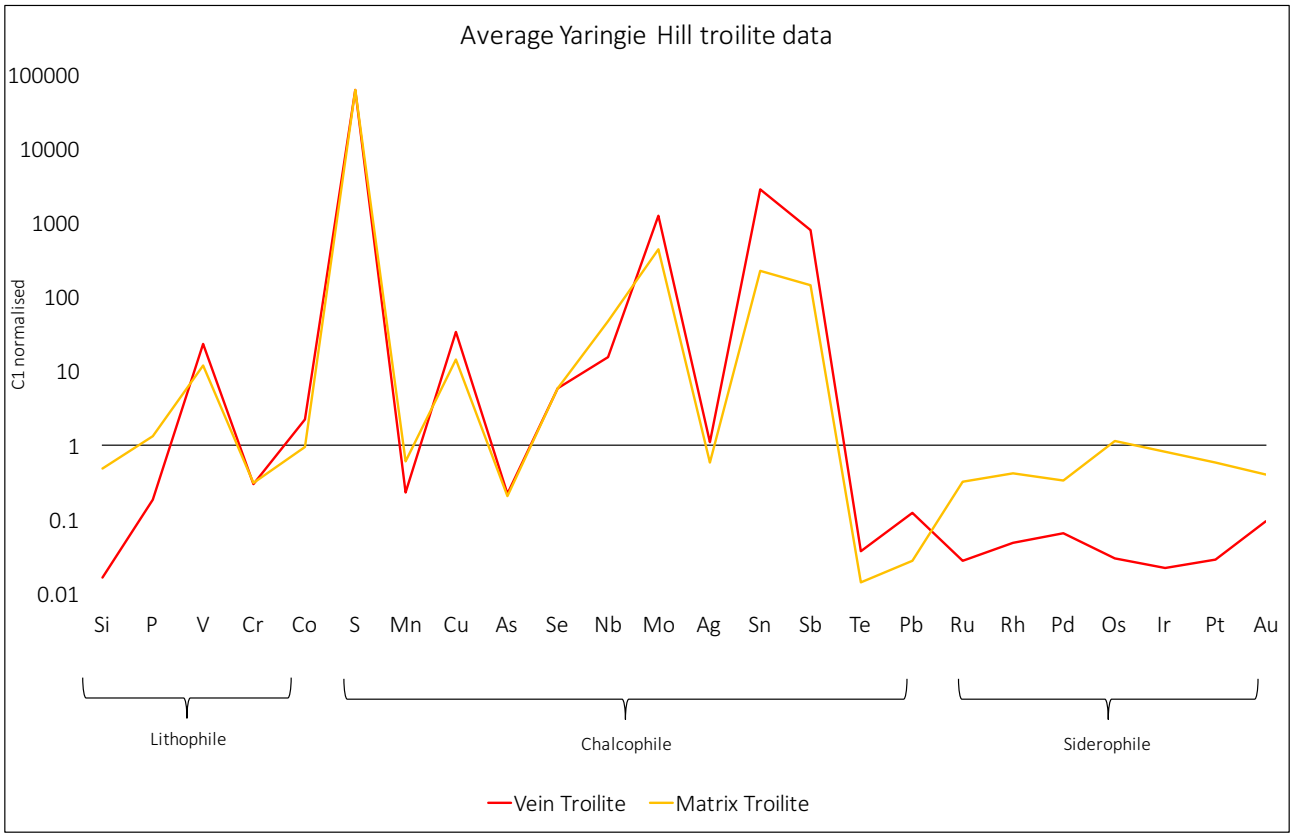

FIGURE 5.5: Average troilite composition for the lithophile, chalcophile and siderophile trace elements of the vein and matrix.

with kD values greater than 1. Exceptions to this are Co, As and Te, who all show affinity for the metallic phase within the matrix and vein. The siderophile elements all show affinity for the metallic phase with kD values less than 1. The exception to this is the two moderately siderophile elements Mn and Mo, who have a preference for the sulphide phase. The partition coefficients for vein metal/matrix metal ($kD_{vm/mm}$) are all close to one, however they show the trend seen previously in Figure 5.4, with the siderophile elements having a stronger preference for the metal in the matrix than the vein.

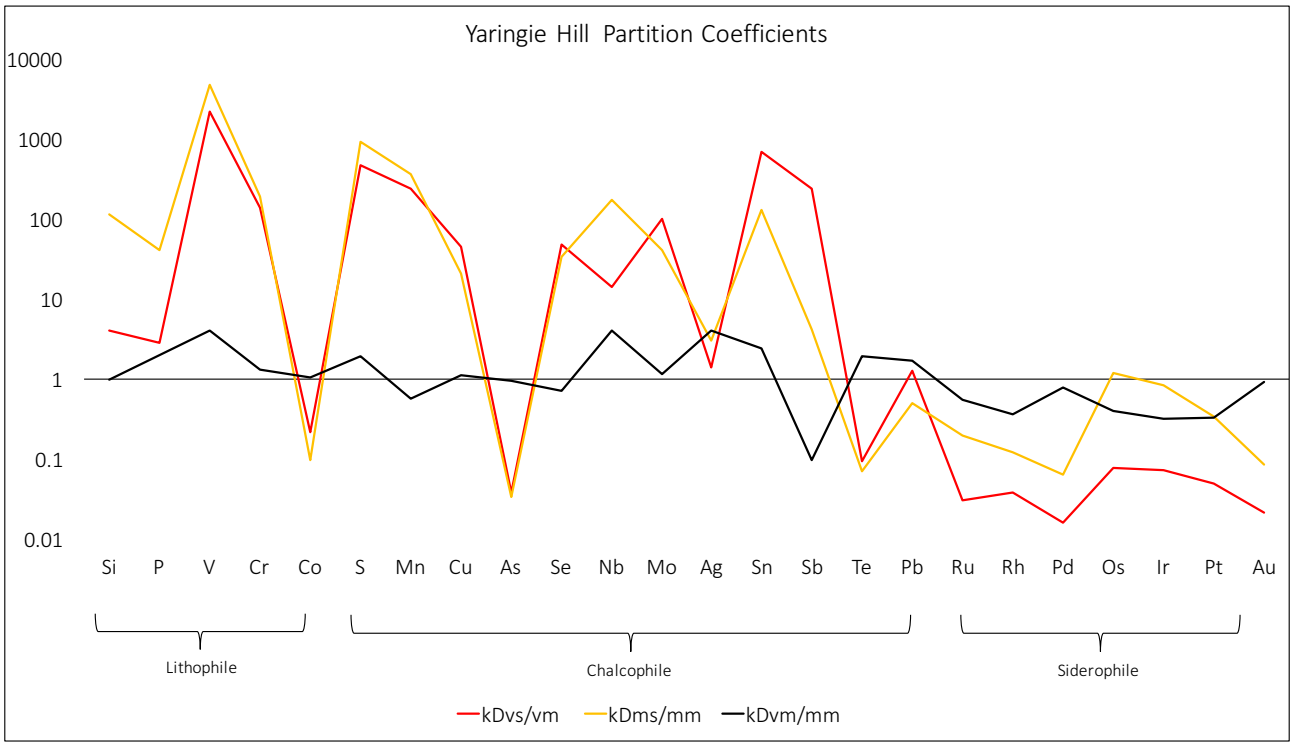

FIGURE 5.6: Partition coefficients calculated for vein sulphide/metal ($kD_{vs/vm}$), matrix sulphide/metal ($kD_{ms/mm}$) and vein metal/matrix metal ($kD_{vm/mm}$).

The average results for the iron and the troilite phase of the Disko Island sample are displayed in Figure 5.7. The raw data for each mineral is displayed within Table 5.4. The iron is expectedly more depleted in the lithophile and chalcophile elements and enriched in the siderophile elements. The exceptions to this are a slightly higher Se content within the iron phase and Rh within the troilite phase.

The sulphide/metal partition coefficients ($kD_{ds/dm}$) for the Disko sample in lithophile, chalcophile and siderophile element order are illustrated in Figure 5.8. Again, the lithophile and chalcophile elements show a strong preference to the troilite phase with $kD_{ds/dm}$ values greater than 1, with the exceptions being Se and Sn. The highly siderophile elements show a strong preference to the iron phase, with the exception of Rh, preferring the sulphide phase. The

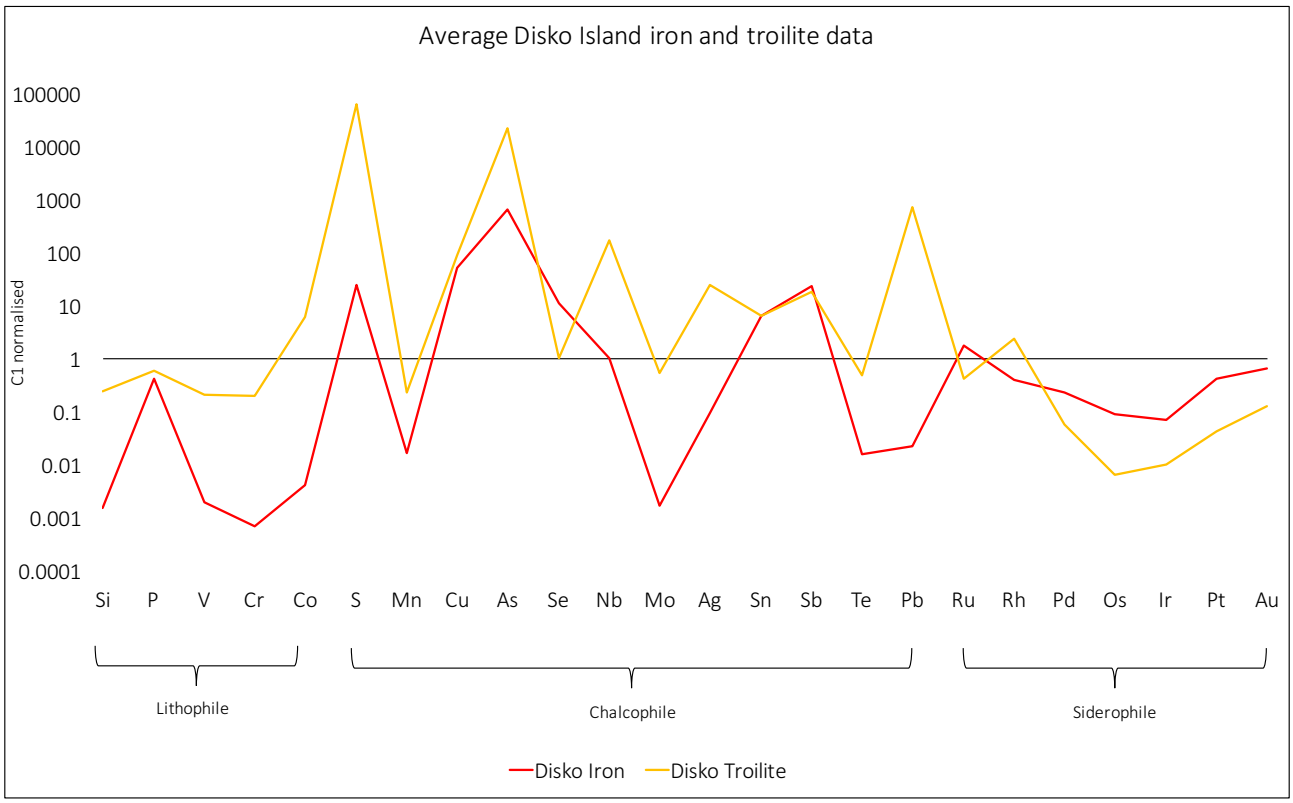

FIGURE 5.7: Average iron and troilite composition for the lithophile, chalcophile and siderophile trace elements of the Disko Island sample.

moderately siderophile elements Mn and Mo both show preference for the troilite phase.

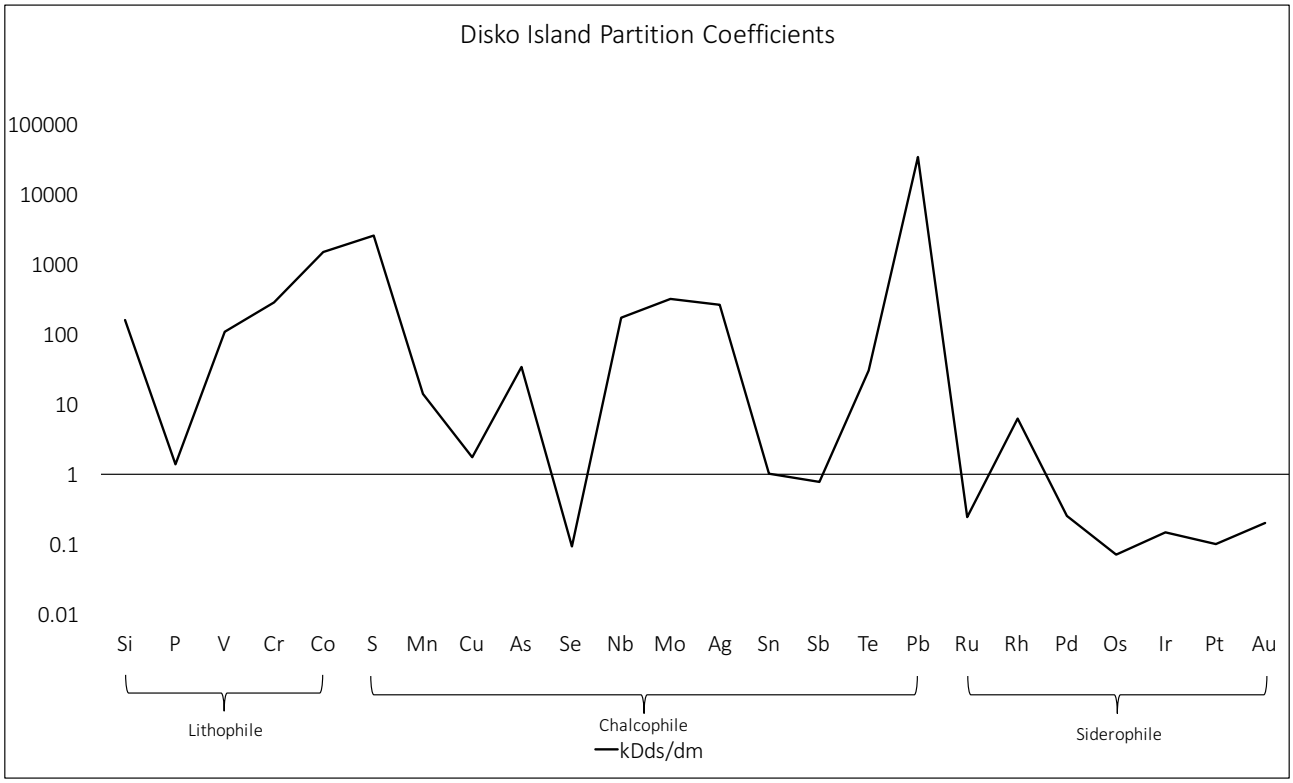

FIGURE 5.8: Partition coefficients calculated for troilite/iron ($kD_{ds/dm}$) within the Disko Island sample.

TABLE 5.2: Average trace element values of vein and matrix kamacite of the Yaringie Hill meteorite

	Vein Kamacite				Matrix Kamacite			
	Average (ppm)	St.Dev	RSD%	n	Average (ppm)	St.Dev	RSD%	n
Si	442.94	245.74	55.48	9	450.52	256.92	57.03	5
P	66.34	40.54	61.11	10	32.87	3.77	11.46	4
S	723.02	400.29	55.36	8	367.68	433.95	118.02	3
V	0.59	0.50	85.03	5	0.14	0.03	20.34	2
Cr	5.68	3.69	64.95	9	4.37	1.45	33.31	4
Mn	1.78	1.18	66.25	11	3.14	3.33	106.14	6
Co	5128.58	177.08	3.45	17	4860.99	124.13	2.55	7
Cu	90.08	14.97	16.62	17	81.56	6.36	7.79	7
As	10.70	2.30	21.50	17	11.38	1.68	14.79	7
Se	2.59	1.29	50.06	2	3.65			1
Nb	0.27	0.15	56.03	2	0.07	0.02	32.64	2
Mo	11.21	4.10	36.57	16	9.58	2.04	21.33	7
Ru	0.64	0.14	21.83	13	1.18	0.57	48.44	7
Rh	0.16	0.05	30.98	16	0.46	0.20	44.25	7
Ag	0.16	0.10	61.55	5	0.04	0.01	26.85	2
Pd	2.25	0.64	28.55	17	2.89	0.30	10.24	7
Sn	6.67	9.39	140.84	16	2.79	1.90	68.11	7
Sb	0.47	0.27	58.08	8	4.76	8.85	185.89	4
Te	0.91	0.79	86.89	4	0.47	0.28	59.31	3
Os	0.19	0.11	56.78	11	0.47	0.37	80.33	7
Ir	0.14	0.06	44.44	12	0.44	0.33	74.35	7
Pt	0.58	0.19	33.04	16	1.77	0.98	55.41	7
Au	0.62	0.10	16.08	17	0.66	0.08	11.56	7
Pb	0.23	0.19	81.75	11	0.14	0.12	88.49	3

TABLE 5.3: Average trace element values of vein and matrix troilite of the Yaringie Hill meteorite

	Vein Troilite				Matrix Troilite			
	Average (ppm)	St.Dev	RSD%	n	Average (ppm)	St.Dev	RSD%	n
Si	1778.61	440.02	24.74	6	51835.16	69302.17	133.70	6
P	188.79	29.95	15.87	6	1346.95	2527.96	187.68	6
S	340230.56	0.01	0.00	6	339118.70	2723.50	0.80	6
V	1323.34	220.02	16.63	6	680.42	537.00	78.92	6
Cr	795.04	385.50	48.49	6	840.73	1267.93	150.81	6
Mn	436.52	392.00	89.80	6	1167.27	1260.61	108.00	6
Co	1107.97	1322.51	119.36	6	472.22	818.32	173.29	6
Cu	4039.80	1832.98	45.37	6	1735.96	1270.76	73.20	6
As	0.41	0.32	79.93	5	0.38	0.32	85.53	6
Se	123.50	3.52	2.85	6	124.70	3.26	2.62	6
Nb	3.78	2.04	54.06	6	11.56	10.22	88.42	6
Mo	1128.30	352.90	31.28	6	393.73	153.56	39.00	6
Ru	0.02	0.01	63.56	4	0.23	0.40	174.36	6
Rh	0.01	0.00	78.56	5	0.06	0.08	149.30	4
Ag	0.22	0.14	62.13	6	0.12	0.14	118.30	6
Pd	0.04	0.03	84.91	6	0.19	0.15	79.81	3
Sn	4713.85	6178.60	131.07	6	370.89	442.07	119.19	6
Sb	113.26	160.56	141.76	6	20.00	30.29	151.47	6
Te	0.09	0.04	48.96	6	0.03	0.02	47.41	5
Os	0.01	0.01	97.54	4	0.56	0.95	169.22	5
Ir	0.01	0.01	107.10	2	0.37	0.57	152.81	5
Pt	0.03	0.02	70.05	3	0.60	1.11	185.04	5
Au	0.01	0.01	103.08	4	0.06	0.03	56.42	3
Pb	0.30	0.35	118.38	6	0.07	0.05	75.92	6

Table 5.4: Average trace element values for iron and troilite of the Disko Island sample

	Disko Iron				Disko Troilite			
	Average (ppm)	St.Dev	RSD%	n	Average (ppm)	St.Dev	RSD%	n
Si	168.84	45.41	26.90	10	27095.21	24012.25	88.62	10
P	444.17	57.84	13.02	10	609.17	402.88	66.14	9
S	136.08	29.99	22.04	10	350237.35	0.03	0.00	10
V	0.11	0.07	62.45	7	12.13	16.54	136.35	10
Cr	1.90	1.53	80.58	10	538.02	222.01	41.26	10
Mn	32.20	16.29	50.58	10	453.38	253.56	55.93	10
Co	2.13	0.28	13.33	10	3103.97	917.21	29.55	10
Cu	6474.61	449.06	6.94	10	11201.40	8825.19	78.79	10
As	1254.51	144.60	11.53	10	42725.73	20324.21	47.57	10
Se	241.38	34.73	14.39	10	22.54	31.60	140.18	10
Nb	0.25	0.09	37.22	5	42.67	15.33	35.93	10
Mo	0.00	0.00	50.21	8	0.50	0.45	89.45	9
Ru	1.29	0.09	6.85	10	0.31	0.28	89.15	10
Rh	0.05	0.00	8.86	10	0.32	0.15	48.46	10
Ag	0.02	0.01	41.12	10	5.12	7.35	143.48	10
Pd	0.13	0.01	11.30	10	0.03	0.03	88.02	10
Sn	10.92	2.00	18.31	10	10.98	12.80	116.58	10
Sb	3.34	0.58	17.25	10	2.58	3.36	130.12	10
Te	0.04	0.01	18.61	2	1.16	1.01	87.30	10
Os	0.05	0.04	83.87	10	0.00	0.00	66.12	4
Ir	0.03	0.04	110.60	10	0.00	0.00	54.61	3
Pt	0.43	0.23	53.71	10	0.04	0.05	110.16	5
Au	0.09	0.02	20.05	10	0.02	0.02	91.43	9
Pb	0.06	0.08	135.89	9	1833.86	3709.39	202.27	10

TABLE 5.5: Yaringie and Disko partition coefficients

	$kD_{vs/vm}$	$kD_{ms/mm}$	$kD_{vm/mm}$	$kD_{ds/dm}$
Si	4.02	115.06	0.98	160.48
P	2.85	40.98	2.02	1.37
S	470.57	922.31	1.97	2573.76
V	2258.27	4774.85	4.11	105.86
Cr	139.92	192.50	1.30	282.57
Mn	245.11	371.55	0.57	14.08
Co	0.22	0.10	1.06	1458.63
Cu	44.85	21.28	1.10	1.73
As	0.04	0.03	0.94	34.06
Se	47.77	34.16	0.71	0.09
Nb	14.26	177.85	4.08	170.97
Mo	100.61	41.10	1.17	317.27
Ru	0.03	0.20	0.55	0.24
Rh	0.04	0.12	0.36	6.09
Ag	1.39	3.02	4.02	259.14
Pd	0.02	0.06	0.78	0.26
Sn	706.86	133.14	2.39	1.01
Sb	243.57	4.20	0.10	0.77
Te	0.09	0.07	1.94	30.59
Os	0.08	1.20	0.40	0.07
Ir	0.07	0.85	0.32	0.14
Pt	0.05	0.34	0.33	0.10
Au	0.02	0.09	0.93	0.20
Pb	1.28	0.51	1.70	33128.82

6 — Discussion

6.1 Source of Vein Metal

In order to understand the mechanisms behind segregation of the metal vein within the Yaringie Hill meteorite, it is necessary to establish using trace element and textural features whether metal within the vein is derived from local in-situ melting or being injected from another source within the ordinary chondrite parent body.

Trace element analysis of the vein and matrix kamacite of the Yaringie Hill Meteorite (Figure 6.1) highlight that the vein is depleted in siderophile elements with respect to the matrix kamacite. This would indicate that the vein is not directly fractionating from the surrounding kamacite of the matrix since the highly siderophile elements would preferentially partition into the melt phase (Rubie et al., 2007), enriching the vein relative to the surrounding matrix. Further evidence of this can be seen within figure 5.5, where the troilite of the vein are depleted in the siderophile elements relative to the matrix. This is emphasized by figure 5.6 whereby partition coefficients for the vein metal/matrix ($kD_{v/m}$) highlight the affinity of siderophile elements for the matrix.

A common textural feature of the vein are apophyses of kamacite that extend into the matrix (Figure 6.2). These could be interpreted as either matrix kamacite melting to form the vein, or injection of the vein into the chondritic material. A laser ablation transect across the vein and into the apophyses was analysed to investigate compositional change and potentially discriminate between these options. A change in trace element concentration within the apophysis is expected if it is locally derived from the matrix, and no change if it is sourced from the vein. Figure 6.3 illustrates the results of the transect, highlighting that siderophile element concentrations within the vein are the same as those of the apophysis. This implies that the vein is being injected into the chondritic material and the apophyses are not the result of locally

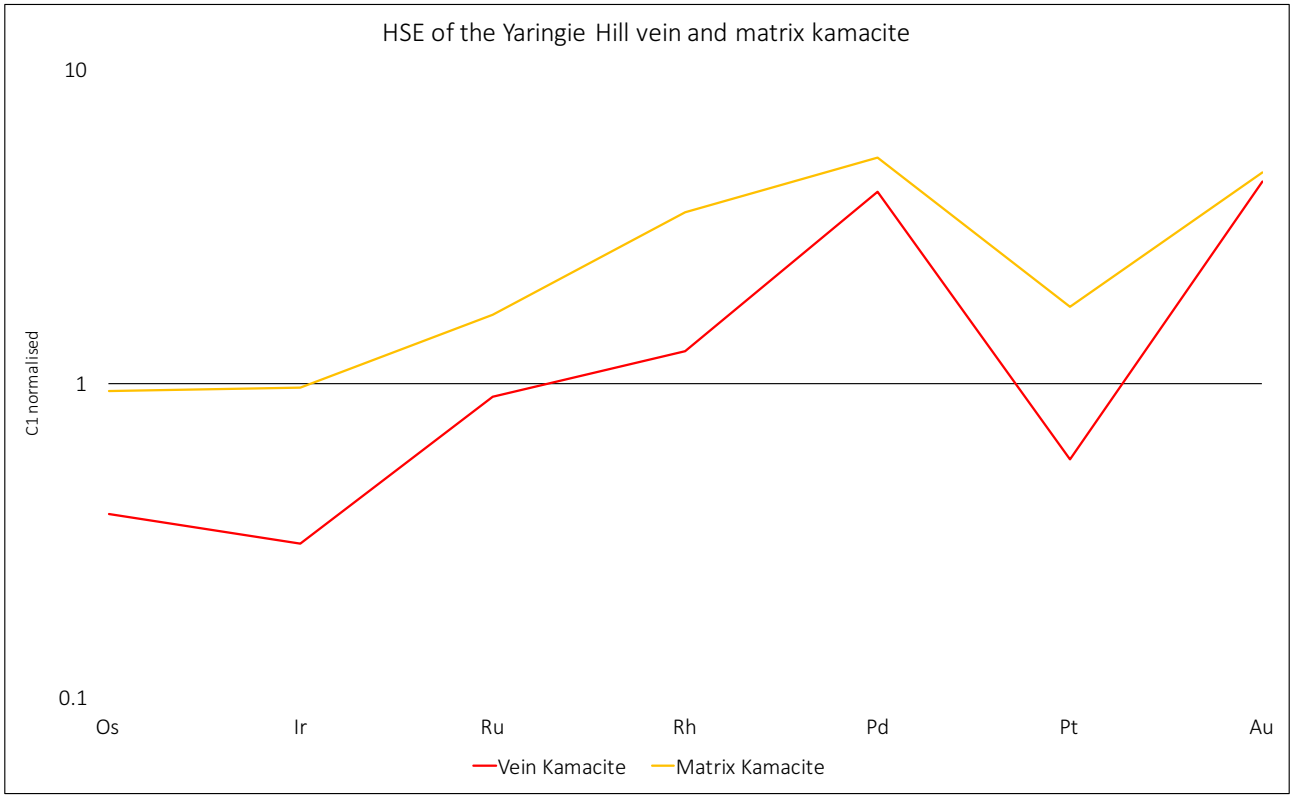

FIGURE 6.1: Highly siderophile elements (HSE) distribution within the kamacite of the matrix and vein of the Yaringie Hill meteorite.

derived chondritic material melting to form the vein.

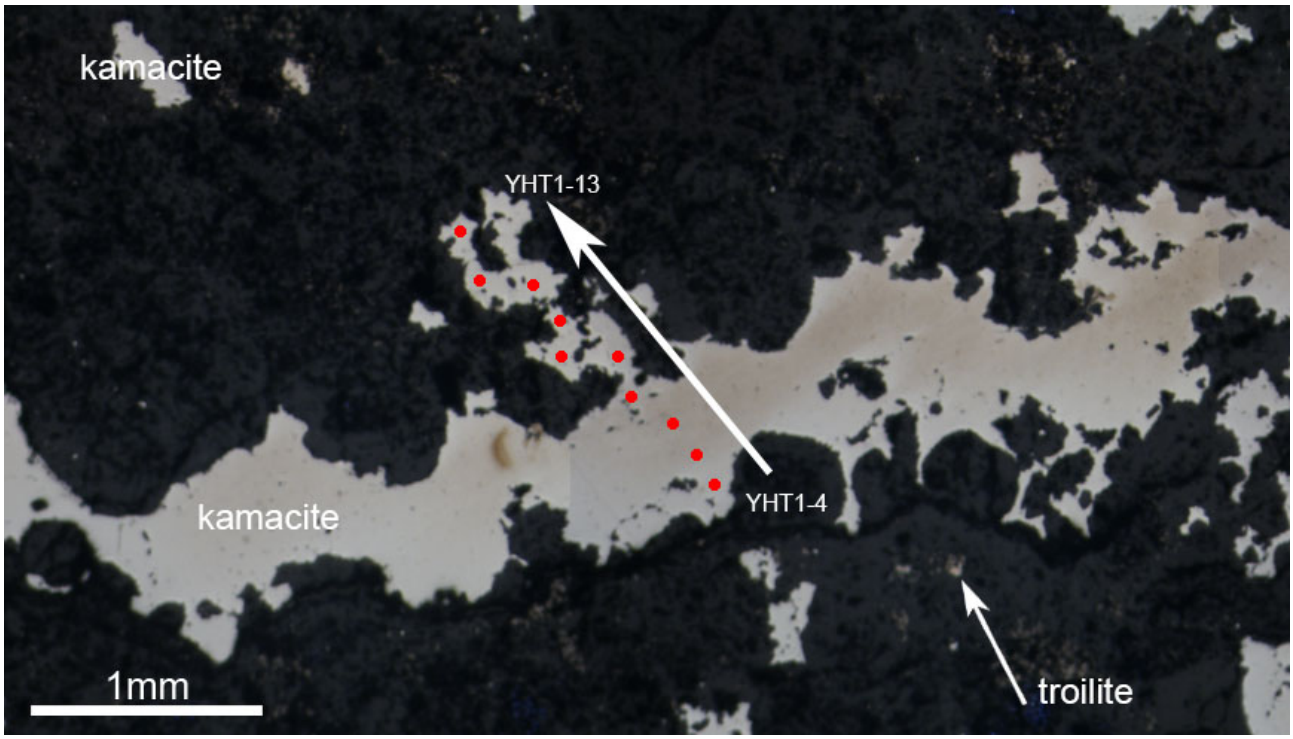

FIGURE 6.2: Reflected light image of the vein showing a transect taken across the vein and into an apophysis. Laser ablation sites YHT1-4 to YHT1-13 are indicated in red.

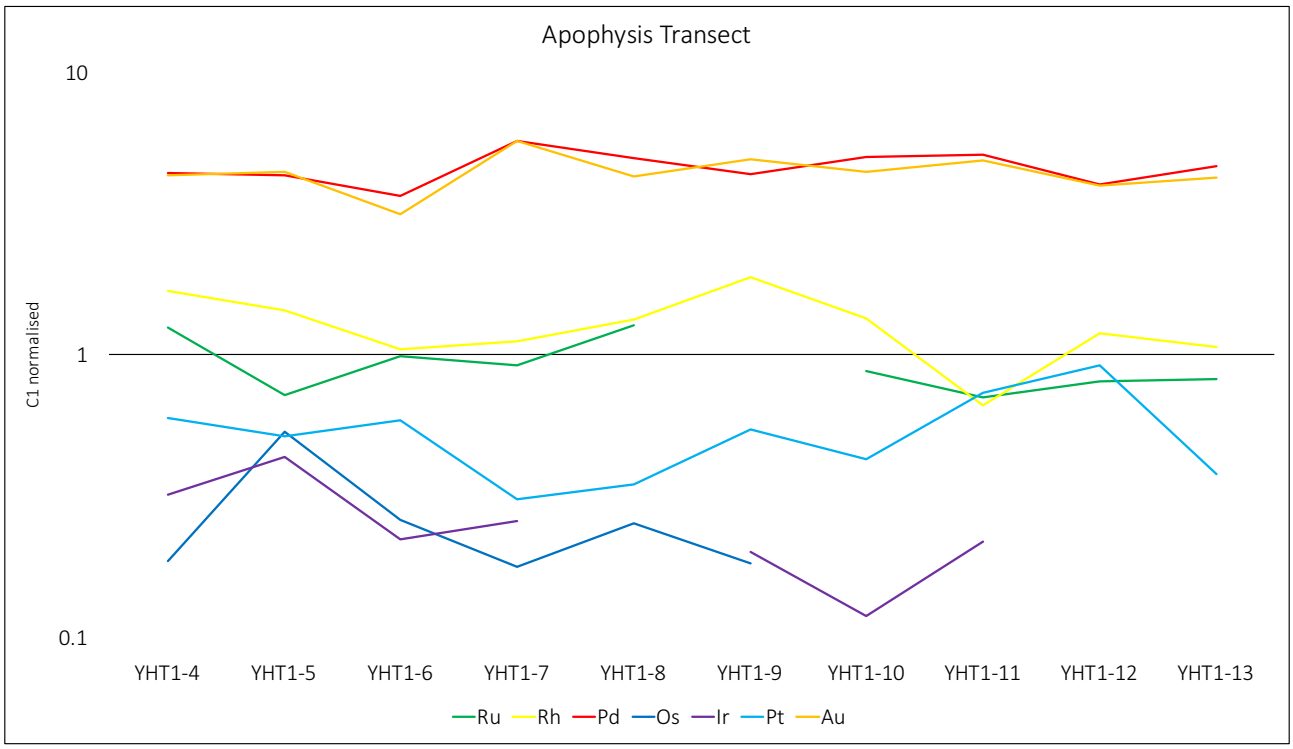

Figure 6.3: HSE data from the centre of the vein (left) into a vein apophysis (right) indicating no systematic variation in abundance with proximity to the silicate host.

Textural relationships obtained by detailed backscatter images and element maps from the SEM further suggests that the vein is not fractionating from the surrounding matrix kamacite, rather the vein is being injected from another source of melt. For example, Figure 6.4 shows the tips of the vein hydraulically fracturing the silicate minerals of the matrix, typical of vein propagation being driven by internal overpressuring (Tomkins et al., 2013). An interesting feature of these vein tips is a change in composition to a higher Ni content than the rest of the vein (Figure 6.5). Similarly, changes in vein tip chemistry have been observed within tholeiitic dyke propagation by Hoek (1994), a result of fractionation due to the flow of residual fluids to the tip. Due to the low gravity of bodies such as asteroids and planetesimals, the flow of melt is primarily controlled due to deformation driven pressure gradients, as the low gravity environment significantly reduces gravitational flow (Tomkins et al., 2013). The viscosity of a melt directly controls the speed and therefore distance that a melt can travel (Tomkins et al., 2013). An FeNi±S melt (0.004 Pa s^{-1}) will travel ~2500 faster than a basaltic melt (~10 Pa s^{-1}, 1250°C) (Tomkins et al., 2013). A pressure gradient created through strong deformation would then be capable of driving a metal vein into an unmelted silicate domain from an area of metallic and silicate melt. The lack of any silicate melt around the vein could therefore indicate that the vein is being injected into the chondritic matrix from another source.

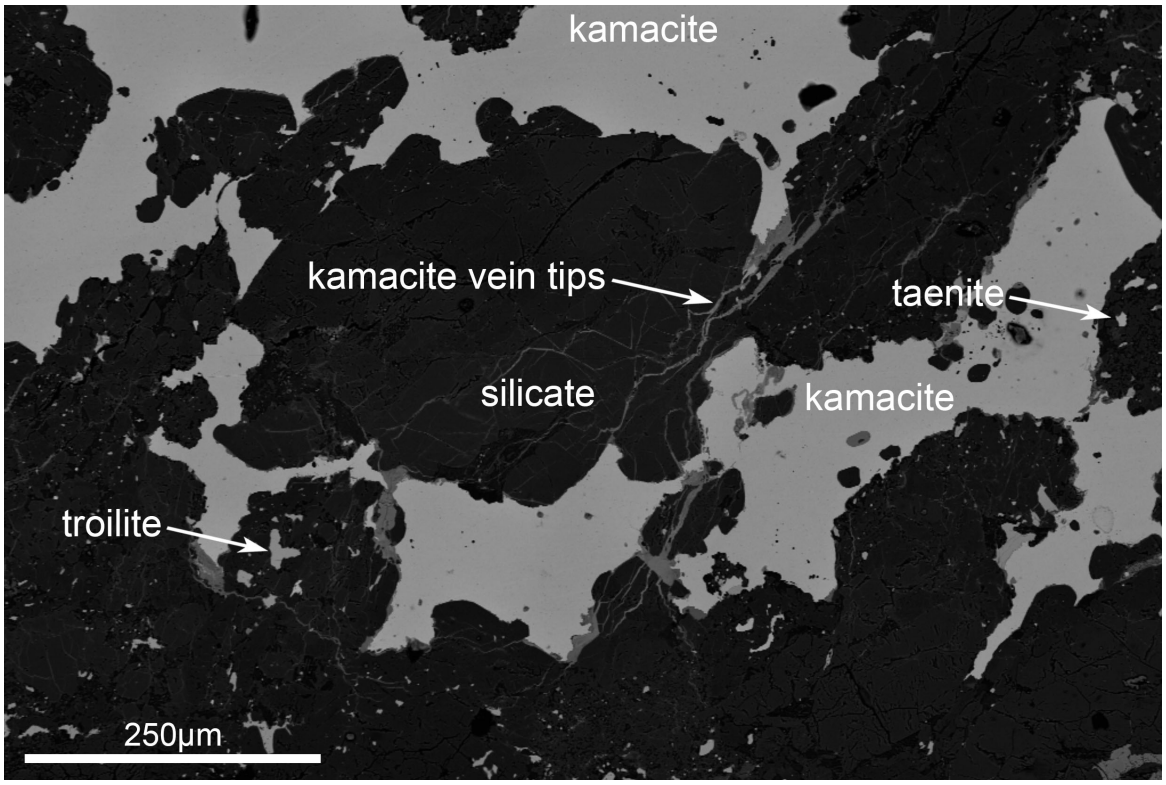

FIGURE 6.4: Backscatter SEM image of propagating metal vein tips fracturing host silicate matrix.

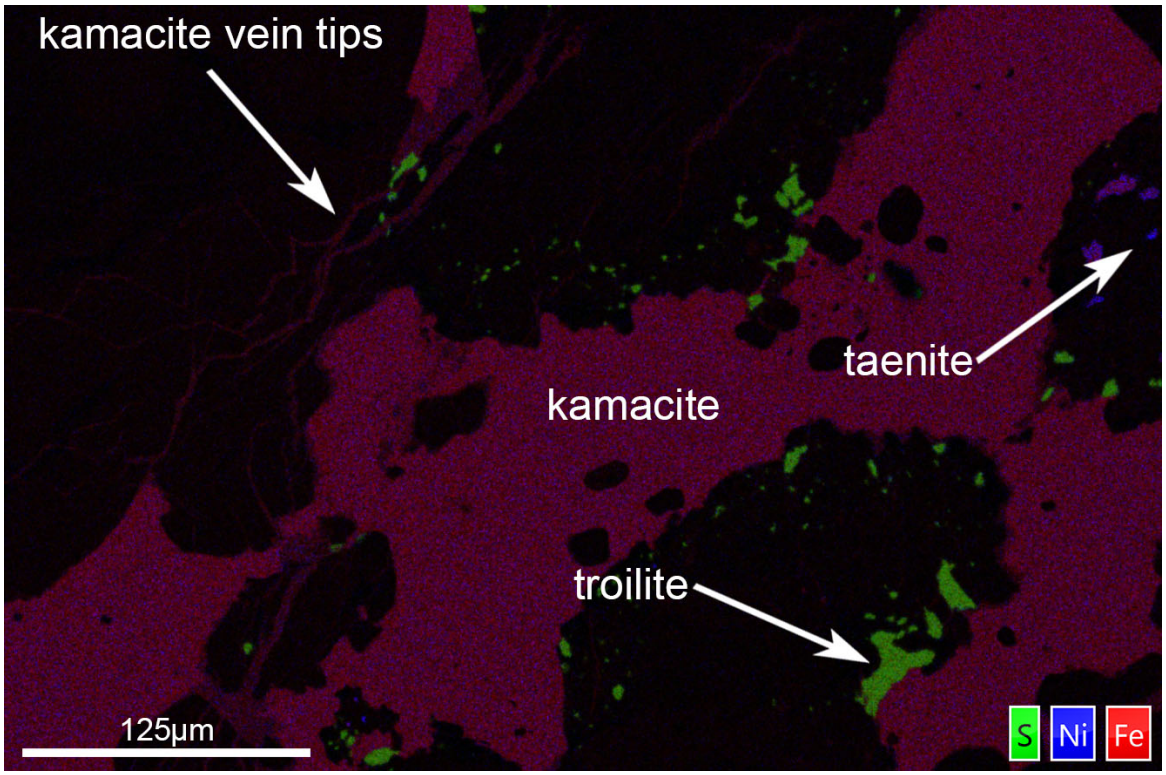

FIGURE 6.5: Fe Ni S element map showing the composition of the vein tips hydraulically fracturing the silicate minerals. Vein tip composition is a kamacite with slightly higher nickel content than the vein, and much lower than matrix hosted taenite.

6.2 Vein Segregation Mechanism

Based on the textural and trace element evidence presented, the vein appears to be a result of injection into the chondritic material as opposed to partial melting of the surrounding matrix

metal. Depletion of the vein in highly siderophile elements relative to matrix metal further rules out a local simple partial melting derivation for vein metal.

The preclusion of a local partial melting model further suggests that the vein could not have formed as a result of a magma ocean scenario. This is because we would expect metal segregated in a magma ocean to be enriched in the incompatible highly siderophile elements relative to the matrix metal of the parent body (Rubie et al., 2007), the inverse of what we see in the Yaringie vein.

We can then infer that the vein must have either formed from a mechanism that results in depletion of less compatible elements during metal-silicate segregation or the vein is sourced from a reservoir of different composition elsewhere within the parent body or accreting solar disc.

The Disko Island sample represents a terrestrial analogue of metal-silicate segregation, reducing FeO and Fe silicates by C in a smelting process. The Disko island sample is the result of a basaltic flow over a coal seam, allowing olivine to be reduced by C, forming native iron as follows the equation $C + MgFeSiO_4 = MgSiO_4 + Fe + CO$ (Warren et al., 2006). Evidence of this as a meteoritic metal-silicate segregation mechanism can be seen in the Ureilite meteorite group. Thus it is reasonable to compare the Yaringie vein metal to demonstrated processes occurring during planetary formation.

The Yaringie kamacite plotted against the Disko Island iron and Bulk Ureilite composition for HSE is displayed in Figure 6.6. The Disko Island iron and Bulk Ureilite are both depleted in HSE concentration relative to the kamacite of the vein and matrix of the Yaringie Hill meteorite. This is consistent with needing a mechanism that can segregate metal with a lower siderophile abundance than the metal of the Yaringie matrix. The Disko Island iron and Bulk Ureilite also show negative Pd and positive Pt anomalies, while the Yaringie metals show the inverse. The Disko Island iron also shows a strong positive Ru anomaly (Figure 6.6).

A strong correlation between the vein and matrix kamacite of the Yaringie Hill meteorite, with the vein generally more depleted in both Pd and Pt relative to the matrix kamacite is highlighted in Figure 6.7. The Disko Island iron and bulk ureilite composition also plot closely, with very similar Pd levels and some depletion in bulk Ureilite Pt relative to the Disko sample.

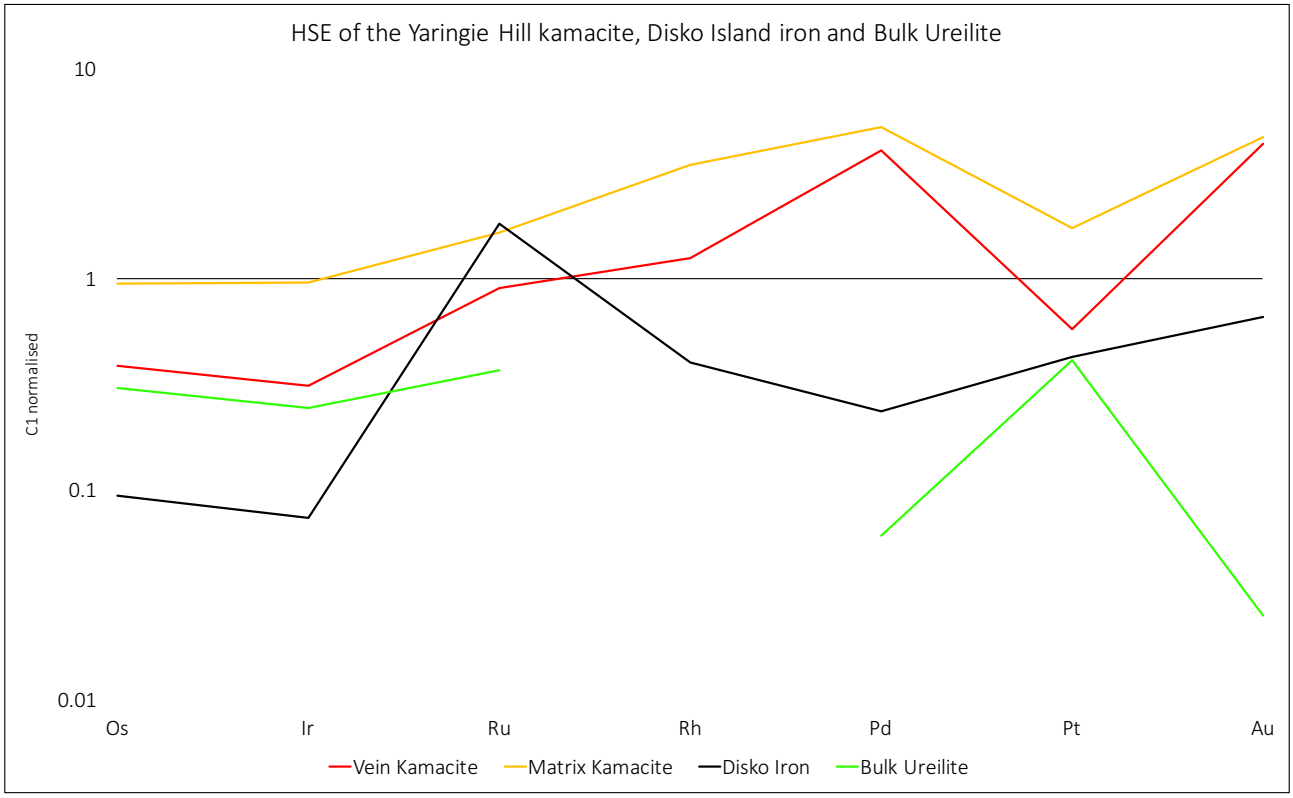

FIGURE 6.6: HSE concentrations within the Yaringie kamacite, Disko iron and bulk Ureilites. Bulk Ureilite data from Warren et al. (2006).

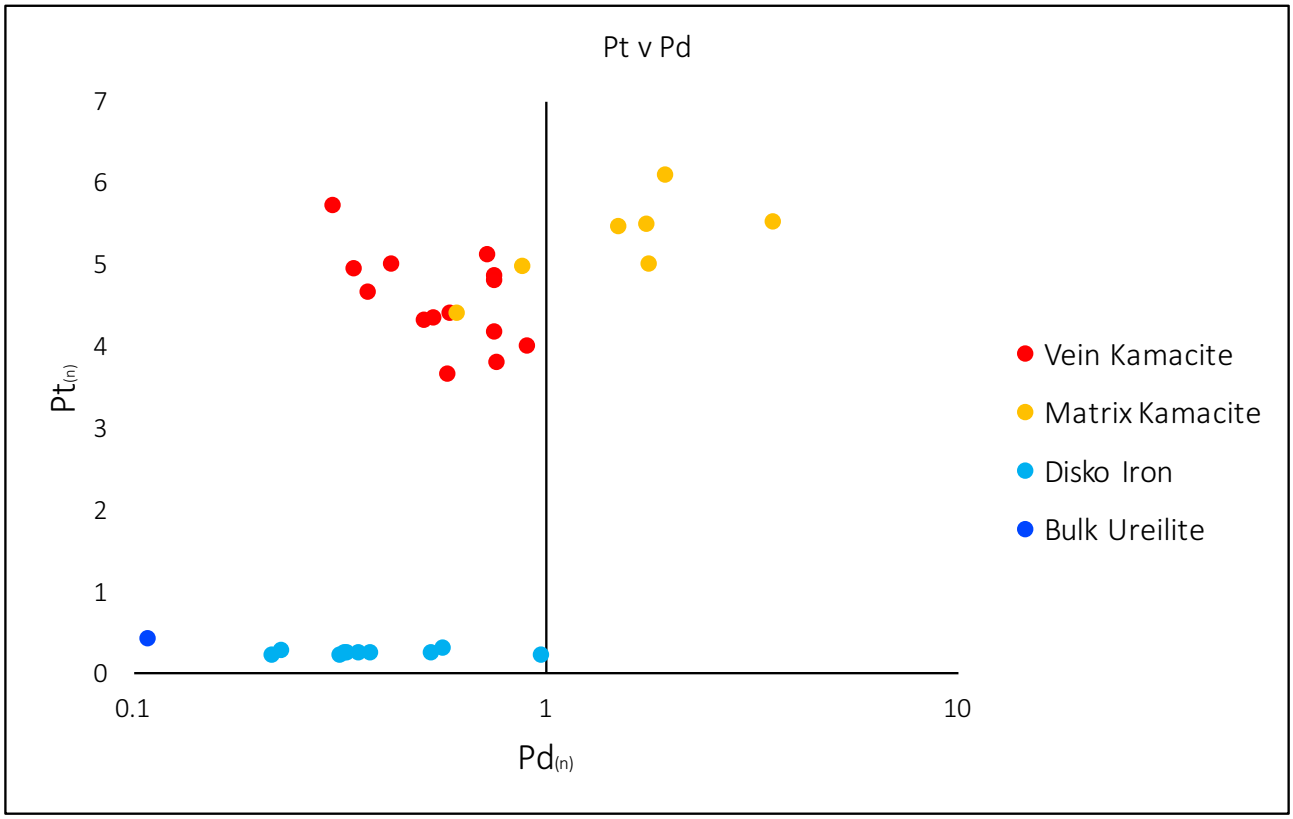

FIGURE 6.7: $Pd_{(N)}$ v $Pt_{(N)}$ for Yaringie Hill kamacite, Disko Island iron and Bulk Ureilite, all normalised to C1 Chondrite. Bulk Ureilite data from Warren et al. (2006).

Based upon the available HSE data we can conclude that while the mechanism that segregated the Yaringie Hill vein resulted in a lower bulk siderophile concentration than the kamacite of the matrix as seen in both smelting analogues, it appears unlikely that smelting was the driving mechanism of segregation. No evidence of Fe rimmed, zoned olivine crystals has been found within the matrix of the Yaringie Hill meteorite from optical and SEM analysis, which would be an indicator of a smelting reaction.

Shock metamorphism caused by accreting material is a metal-silicate segregation mechanism by which temperatures would be great enough to melt both metal and silicate, while providing a transportation system for the melt through pressure gradients resulting in vein propagation (Tomkins et al., 2013). Such a model is consistent with the combination of trace element and textural analysis of the vein, and hence agrees with the interpretation that the vein is a result of injection into previously undifferentiated chondritic material.

Optical analysis of the silicates within the matrix show undulatory extinction of olivines, pyroxenes and plagioclase, as well as the presence of planar fracturing of olivine crystals. Tappert et al. (2009) has classified the Yaringie Hill meteorite to have been weakly shocked up to stage S3 under the classification scheme of Stöffler et al. (1991). This indicates the Yaringie Hill meteorite experienced pressure deformation of 10-20GPa. The kamacite vein seen within the Yaringie Hill meteorite are also a rare feature of S3 deformation (Stöffler et al., 1991).

While silicate melt would occur at the site of a large impact, its absence within the Yaringie Hill meteorite does not preclude the vein being formed though shock metamorphism. This is due to the viscosity of melt controlling the speed and therefore distance a melt can flow, allowing a low viscosity FeNi±S melt to travel further than the higher viscosity silicate melt (Tomkins et al., 2013). This would result in metallic melts being able to migrate away from silicate melt into undifferentiated chondritic material. In this context Yaringie Hill could simply represent the distal portion of a shock metamorphic melt induced system.

The expulsion of sulphides from the metallic melt is a key indicator of shock metamorphism (Tomkins et al., 2013). On cooling, S within the metallic melt becomes wetting toward olivine, while the Fe metal remains non-wetting. This results in a capillary action within microfractures in the silicate drawing the S dominant melt out of the metallic phase. Vein networks of troilite are then formed as the S rich melt reacts with small Fe grains as it crystallises (Tomkins

et al., 2013). Optical and SEM analysis shows networks of troilite outside of the vein are not a feature of the Yaringie Hill meteorite, instead troilite is present as rounded immiscible grains wholly within the vein itself (Figure 6.8). While the Yaringie Hill meteorite clearly displays signs of experiencing shock deformation, it seems unlikely based on trace element abundances and sulphide behaviour that the vein is simply a result of shock metamorphism.

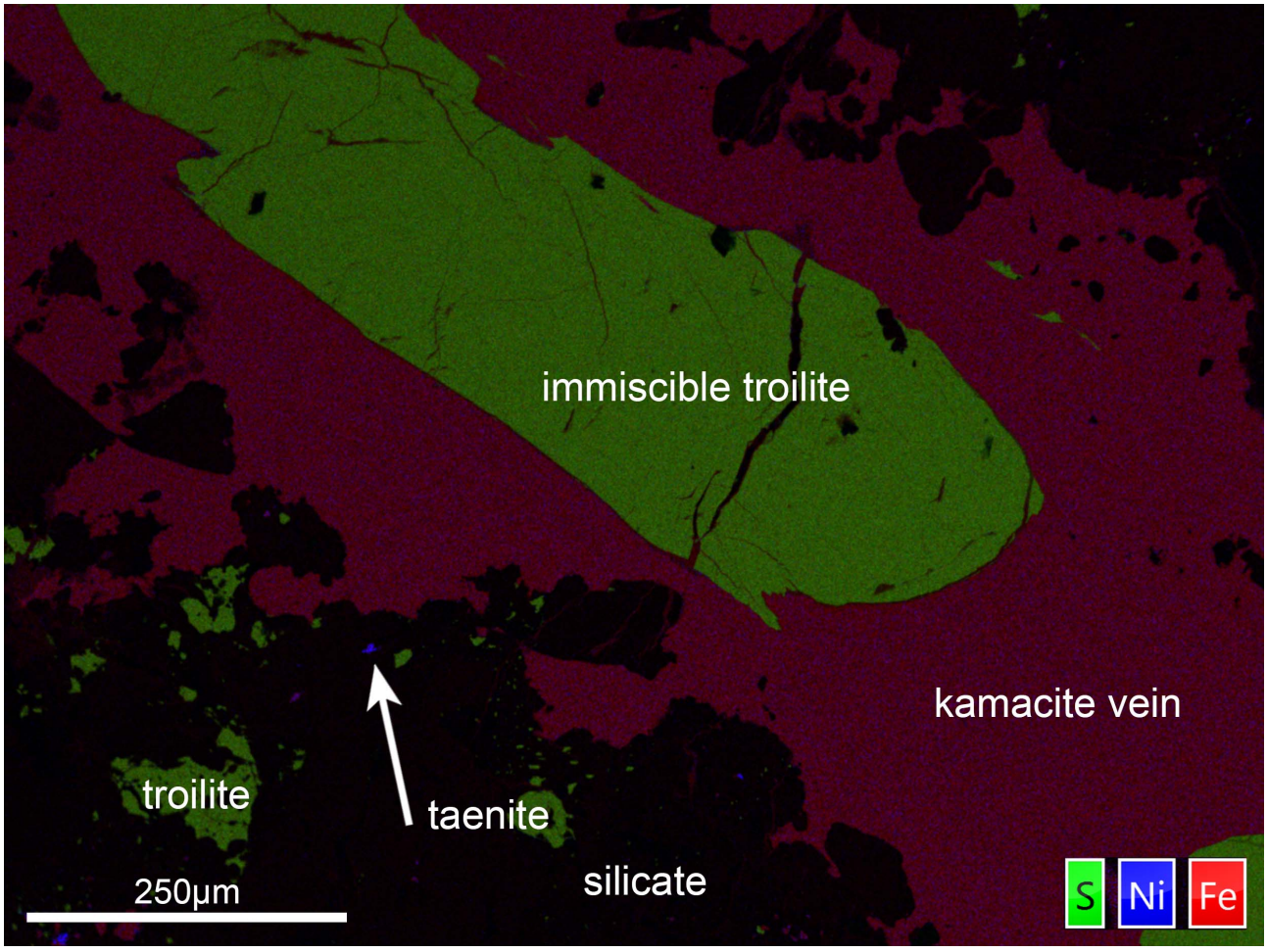

FIGURE 6.8: Fe Ni S element map illustrating immiscible troilite grains within the kamacite vein of the Yaringie Hill meteorite.

Alternatively, metal within ordinary chondrites has been observed to form 2-30mm nodules and metal veins without associated silicate melting (Tomkins et al., 2013; Rubin, 2002, 1999; Kong et al., 1998; Widom et al., 1986). These veins and nodules are depleted in the highly refractory elements Re, Os, Ir, Ru, Rh and Pt. However they are not depleted in the normally refractory W and Mo, nor common siderophiles Fe, Ni and Co or volatile siderophiles Au, As and Sb relative to bulk metal composition (Rubin, 1999). It is currently thought that these veins and nodules are the result of vapour deposition after impact vapourisation (Rubin, 1999; Widom et al., 1986). A fractional condensation model proposed by Rubin (1999), suggests

that during an impact, both metal and silicate are vapourised. The moderately volatile W and Mo are then oxidised by the silicate vapour, along with Re and Os which would become partially oxidised. The unoxidised refractory siderophile elements, along with a small fraction of Re and Os, on cooling condense first onto pre-existing grains or as a mobile melt. Transport then occurred condensing the residual vapour containing the common siderophiles, volatile siderophiles and W, Mo Re and Os oxides into fractures. Reduction of these oxides occurred either on cooling or during annealing of the parent body.

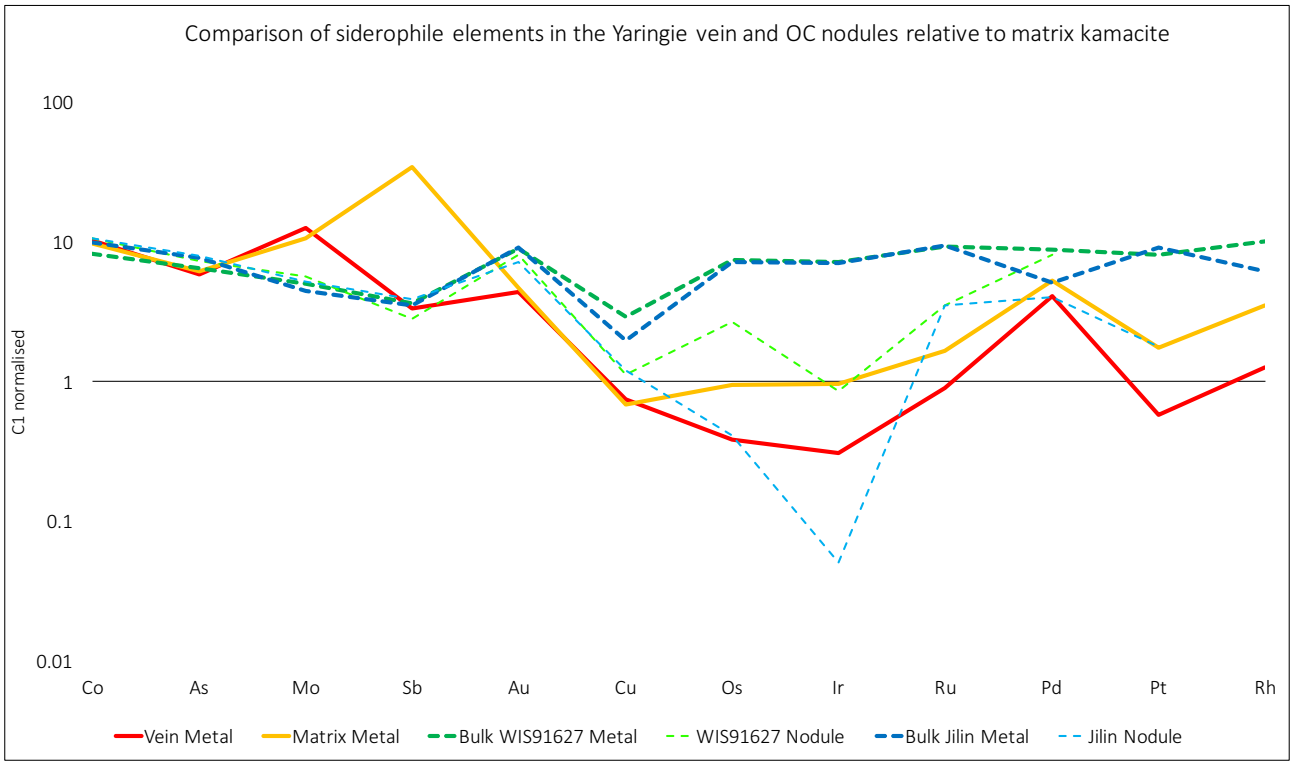

Figure 6.9: Yaringie matrix and vein kamacite compared with WIS91627 and Jilin bulk metal analysis and metal nodule analysis. The metal nodules are interpreted to be the result of vapour deposition. WIS91627 and Jilin bulk metal and metal nodule data from Kong et al. (1998).

The Yaringie kamacite can be seen plotted against bulk metal and nodule metal analysis from the WIS91627 and Jilin Ordinary chondrites in Figure 6.9. The Yaringie vein is depleted relative to the matrix in the HSE, while Co, As and Au are similar to matrix concentrations. The same trends can be seen with respect to the bulk metal and metal nodules of the WIS91627 and Jilin Ordinary chondrites, however the differences lie in Sb being depleted relative to matrix metal, and Cu having the same concentration as the matrix metal. These differences could possibly be a result of later processing within the parent body.

Based on the trace element patterns of depleted highly siderophile elements relative to bulk

composition and the depleted kamacite forming a vein, it seems very plausible that the metal-silicate segregation mechanism forming the kamacite vein within the Yaringie Hill meteorite is a result of vapour deposition. It should be recognised however as noted by Tomkins et al. (2013), that the vapour condensation model proposed by Rubin (1999); Widom et al. (1986) has not yet been supported by any physical evidence or a thermodynamic argument. Notwithstanding, the fractionation's in HSE observed between the vein and the matrix in Yaringie Hill meteorite are likely to share a common origin with that observed in Jilin and WIS91627.

6.3 Core Compositions

One of the main difficulties in understanding the Earth's core formation is our inability to directly sample it. Instead we rely on constraints provided by geophysical and geochemical modelling. Iron meteorites however allow us to analyse the remnant cores of early planetesimals that differentiated early within the solar system before subsequently being destroyed (Rubie et al., 2007). By comparing the vein kamacite of the Yaringie Hill meteorite with the compositions of various iron meteorites, we can better understand the degree to which various metal-silicate segregation mechanisms play a role in core formation.

Figure 6.10 compares the metals of the Yaringie Hill meteorite against IVB, IIIAB iron meteorites and the Cumulus Ridge and Brenham Pallasite.

IIIAB irons have been interpreted to be the result of a magmatic fractional crystallisation series, resulting in greater PGE abundance within the early products (Wabar and Henbury), while the latest stages of fractional crystallisation resulted in strong depletion of the PGEs overall, particularly with respect to Os and Ir (Grant and Mt Edith) (Mullane et al., 2004).

In contrast, the Brenham pallasite is a main group pallasite that has been interpreted to have formed from a depleted system synchronous with the formation of the IIIAB iron meteorites (Mullane et al., 2004). This indicates a genetic connection between the two where the pallasite melt became isolated from the IIIAB source, which then continued to further fractionate (Mullane et al., 2004). The Cumulus Ridge pallasite is also a main group pallasite that displays very similar HSE patterns to Brenham. Danielson et al. (2009) however argued that the Cumulus Ridge pallasite did not form from the same parent body as the IIIAB meteorites, instead at the core-mantle boundary of another asteroid. Regardless, the pallasites appear to

share a characteristic depletion in Os and Ir along with the late stage subset of the IIIAB meteorites.

The IVB group of meteorites are thought to represent a fractionally crystallised core of a planetesimal that accreted a high proportion of PGE rich metal grains formed from high temperature volatilization/condensation processes within the early solar nebular (Campbell and Humayun, 2005). They contain on average the highest abundances of refractory siderophile elements in the iron meteorite group (Campbell and Humayun, 2005).

We can see that neither the Yaringie vein nor the matrix metals show any direct correlation with any of the irons or pallasites. This is perhaps indicative of the degree of processing that is undergone between initial differentiation to final core composition. Interestingly however, while the most plausible mechanism for vein differentiation appears to be through vapour deposition as a result of impact vaporisation, the vein appears to be transitional towards the later stage, heavily fractionated IIIAB meteorites and pallasites. Thus it seems that in addition to metal-silicate segregation mechanisms, the composition of the accreted material plays a significant role in controlling the resultant composition of the core.

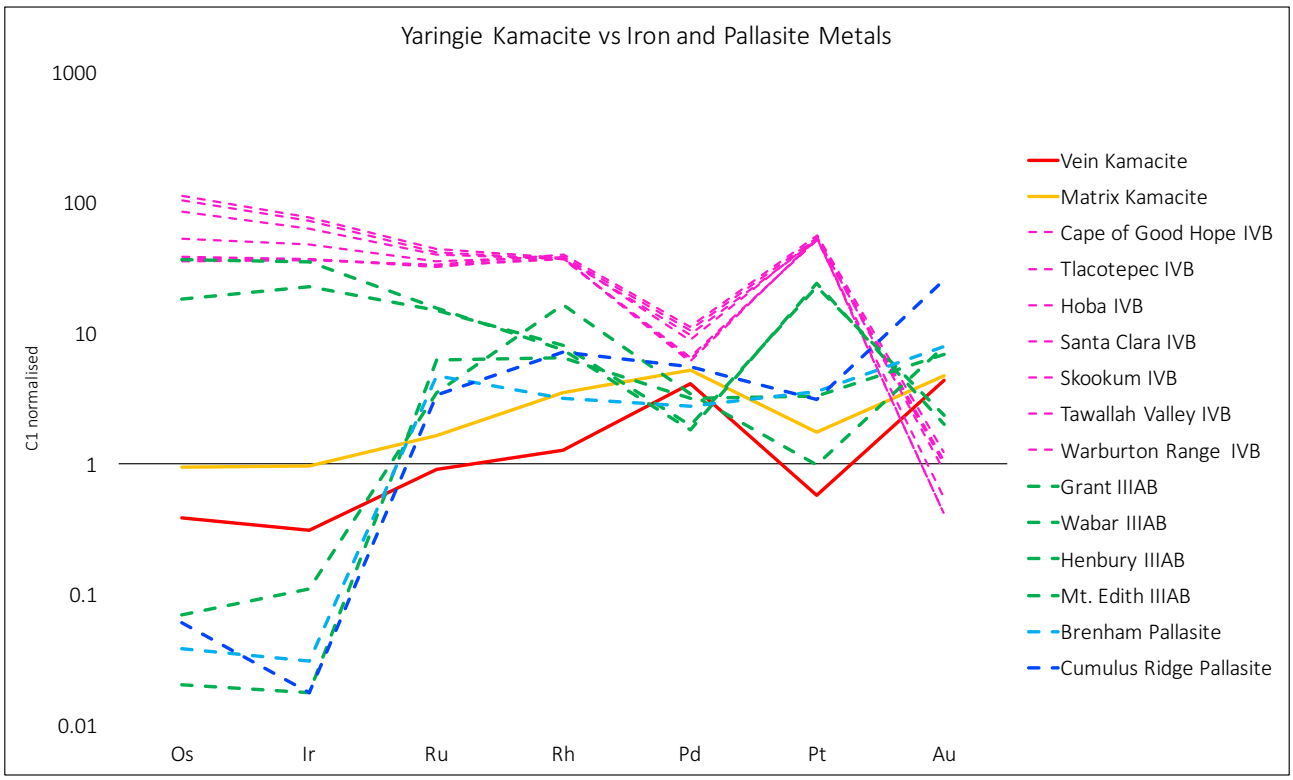

Figure 6.10: Comparison of Yaringie Hill kamacite with IVB, IIIAB iron meteorites and the Cumulus Ridge and Brenham Pallasites. IVB data from Campbell and Humayun (2005), IIIAB and Brenham data from Mullane et al. (2004), Cumulus Ridge data from Danielson et al. (2009).

6.4 Summary

Based on the available textural and trace element data it appears the kamacite vein within the Yaringie Hill meteorite has been formed as a result of vapour deposition resulting from impact vapourisation.

Textural analysis and trace element data appear to agree that injection of a mobile melt rather than the partial melting of local chondritic matrix metal resulted in the formation of the vein. Trace element analysis and comparison with other metal-silicate-sulphide segregation mechanisms also indicates that smelting reactions, a magma ocean scenario and shock metamorphism all appear to disagree with the relative HSE fractionation patterns between the metal in the vein and the matrix. Vapour deposition however provides a mechanism whereby a mobile melt depleted in the HSE relative to matrix metal compositions could form, and be injected into the chondritic matrix.

Comparison between the segregated Yaringie metal, iron meteorites and pallasites highlights that the metal in the vein doesn't match the analogous later stages of core formation. However it could suggest that the extreme depletions of HSE that we see in the IIIAB irons and pallasites may not only be the result of late stage fractional crystallisation (Mullane et al., 2004), but also due to the input of iron sources within the parent body that were differentiated by segregation mechanisms like vapour deposition.

7 — Conclusions

The Yaringie Hill meteorite has granted us a unique opportunity to study the early stages of metal-silicate-sulphide segregation within the ordinary chondrite parent body. A multi-faceted geochemical approach combining textural analysis, major, minor and trace element geochemistry has allowed us to investigate the genesis and mechanisms behind the prominent kamacite vein which cross-cuts the entire Yaringie Hill meteorite. An understanding of the mechanisms behind the vein is important as it represents the early stages of the planetary building cycle, in particular, the beginnings of core formation.

Based on the data collected by this study, and the comparison with published literature values, we have been able to determine;

1. Trace element abundance and partition coefficients within the metals and sulphides of the Yaringie Hill meteorite. This has enabled quantification of the fractionation undergone on the ordinary chondrite parent body resulting from the differentiation of the kamacite vein.

2. Trace element abundance and partition coefficients for metals and sulphides formed via a smelting process for the Disko Island sample.

3. The cross-cutting vein of the Yaringie Hill meteorite appears to have resulted from injection of a mobile melt into the undifferentiated ordinary chondrite matrix, opposed to partial melting of the local kamacite of the matrix. This has been supported by textural features that indicate injection of melt, hydraulically fracturing the silicates of the matrix, and trace element data showing the vein kamacite to be depleted in HSE relative to the matrix. This is the inverse of what would be expected from a partial melting model.

4. The vein appears to be neither the result of shock metamorphism as previosly interpreted (Tappert et al., 2009), nor smelting. Trace element patterns for smelting based off the analogous Disko Island sample and bulk Ureilite composition indicate that while smelting

provides a mechanism for HSE depletion relative to C1 chondrite, it doesn't appear to have controlled the metal-silicate-sulphide segregation within the Yaringie Hill meteorite. Shock metamorphism provides a mechanism of melt propagation needed to form the Yaringie Vein, however the absence of sulphide expulsion from the vein on crystallisation would indicate that it isn't responsible for the veins formation.

5. Vapour deposition as a result of impact vapourisation as proposed by Rubin (1999); Widom et al. (1986) seems to provide the most plausible metal-silicate-sulphide mechanism for the formation of the Yaringie Hill vein. Bulk metal and metal nodule data from ordinary chondrites analysed by Kong et al. (1998) and interpreted to be formed through vapour deposition show very similar HSE depletions and no depletion within some of the more common and volatile siderophile elements as is seen in the kamacite of the Yaringie vein and matrix. This would indicate at the very least a common origin between the ordinary chondrite nodules and the Yaringie vein.

6. The segregated kamacite of the Yaringie vein is very different in HSE abundance relative to the IIIAB and IVB iron meteorites and pallasites. The vein kamacite however does appear transitional in its HSE patterns to the more depleted IIIAB metal and pallasites which have been interpreted to represent the later stages of fractional crystallisation (Mullane et al., 2004). This could perhaps indicate that the strong depletion seen in these meteorites may not be only due to fractional crystallisation, but the input of iron sources into the core that have been differentiated though mechanisms like vapour deposition.

Future directions for this research should strongly focus toward building a larger body of literature surrounding the vapour deposition model and determining if it results in metal equilibrated with the surrounding silicate. As noted by Tomkins et al. (2013), no physical evidence or thermodynamic argument has been put forward to fully support the vapour deposition model put forward by Rubin (1999); Widom et al. (1986). The importance of this lies in that ordinary chondrites make up the single largest meteorite group found on Earth. This suggests that the metal-silicate-sulphide segregation mechanisms that we see operating on this body would have been perhaps some of the most common and potentially most important segregation mechanisms operating within the early stages of the planetesimal building cycle. These mechanisms therefore may be the most important to focus on when trying to understand planetary core formation.

References

Olivier Alard, William L Griffin, Jean Pierre Lorand, Simon E Jackson, et al. Non-chondritic distribution of the highly siderophile elements in mantle sulphides. *Nature*, 407(6806):891, 2000.

Joel Baker, Martin Bizzarro, Nadine Wittig, James Connelly, and Henning Haack. Early planetesimal melting from an age of 4.5662 gyr for differentiated meteorites. *Nature*, 436 (7054):1127, 2005.

William F Bottke, David Nesvornỳ, Robert E Grimm, Alessandro Morbidelli, and David P O'brien. Iron meteorites as remnants of planetesimals formed in the terrestrial planet region. *Nature*, 439(7078):821, 2006.

Andrew J Campbell and Munir Humayun. Compositions of group ivb iron meteorites and their parent melt. *Geochimica et Cosmochimica Acta*, 69(19):4733–4744, 2005.

Tais W Dahl and David J Stevenson. Turbulent mixing of metal and silicate during planet accretionand interpretation of the hf–w chronometer. *Earth and Planetary Science Letters*, 295(1):177–186, 2010.

Lisa R Danielson, Kevin Righter, and Munir Humayun. Trace element chemistry of cumulus ridge 04071 pallasite with implications for main group pallasites. *Meteoritics & Planetary Science*, 44(7):1019–1032, 2009.

N Dauphas, DL Cook, A Sacarabany, Carla Froehlich, AM Davis, M Wadhwa, A Pourmand, T Rauscher, and R Gallino. Iron 60 evidence for early injection and efficient mixing of stellar debris in the protosolar nebula. *The Astrophysical Journal*, 686(1):560, 2008.

Geoffrey F Davies. Heat deposition and retention in a solid planet growing by impacts. *Icarus*, 63(1):45–68, 1985.

Renaud Deguen, Peter Olson, and Philippe Cardin. Experiments on turbulent metal-silicate mixing in a magma ocean. *Earth and Planetary Science Letters*, 310(3):303–313, 2011.

Sarah Gilbert, Leonid Danyushevsky, Philip Robinson, Cora Wohlgemuth-Ueberwasser, Norman Pearson, Dany Savard, Marc Norman, and Jacob Hanley. A comparative study of five reference materials and the lombard meteorite for the determination of the platinum-group elements and gold by la-icp-ms. *Geostandards and Geoanalytical Research*, 37(1):51–64, 2013.

Matthieu Gounelle, Anders Meibom, Patrick Hennebelle, and Shu-ichiro Inutsuka. Supernova propagation and cloud enrichment: A new model for the origin of 60fe in the early solar system. *The Astrophysical Journal Letters*, 694(1):L1, 2009.

Johan Dick Hoek. *Mafic dykes of the Vestfold Hills, East Antarctica. An analysis of the emplacement mechanism of tholeiitic dyke swarms and of the role of dyke emplacement during crustal extension.* Utrecht University, 1994.

Hiroki Ichikawa, Stéphane Labrosse, and Kei Kurita. Direct numerical simulation of an iron rain in the magma ocean. *Journal of Geophysical Research: Solid Earth*, 115(B1), 2010.

AJG Jurewicz, David W Mittlefehldt, and JH Jones. Experimental partial melting of the allende (cv) and murchison (cm) chondrites and the origin of asteroidal basalts. *Geochimica et Cosmochimica Acta*, 57(9):2123–2139, 1993.

S Karato and VR Murthy. Core formation and chemical equilibrium in the Earth .1. Physical considerations. *Physics of the Earth and Planetary Interiors*, 100(1-4):61–79, MAR 1997. Joint Meeting of International-Association-of-Seismology-and-Physical-Properties-of-Earth -Interior / International-Association-Volcanology-and-Geochemistry-of-Earth, BOULDER, CO, JUL, 1995.

W. Klöck, H. Palme, and H. J. Tobschall. Trace elements in natural metallic iron from disko island, greenland. *Contributions to Mineralogy and Petrology*, 93(3):273–282, Jul 1986.

Eiichiro Kokubo and Shigeru Ida. On runaway growth of planetesimals. *Icarus*, 123(1):180–191, 1996.

Ping Kong, Mitsuru Ebihara, and Xiande Xie. Reevaluation of formation of metal nodules in ordinary chondrites. *Meteoritics & Planetary Science*, 33(5):993–998, 1998.

T Kunihiro, AE Rubin, KD McKeegan, and JT Wasson. Initial Al-26/Al-27 in carbonaceous-chondrite chondrules: Too little Al-26 to melt asteroids. *Geochimica et Cosmochimica Acta*, 68(13):2947–2957, JUL 2004.

HP Longerich. Laser ablation inductively coupled plasma mass spectrometric transient signal data acquisition and analyte concentration calculation. *J. Anal. At. Spectrom.*, 9:899–904, 1996.

HP Longerich, D Günther, and SE Jackson. Elemental fractionation in laser ablation inductively coupled plasma mass spectrometry. *Fresenius' journal of analytical chemistry*, 355(5):538–542, 1996.

William F McDonough and S-S Sun. The composition of the earth. *Chemical geology*, 120(3-4): 223–253, 1995.

HJ Melosh. Giant impacts and the thermal state of the early earth. *Origin of the Earth*, 1: 69–83, 1990.

RK Mishra, JN Goswami, S Tachibana, GR Huss, and NG Rudraswami. 60fe and 26al in chondrules from unequilibrated chondrites: implications for early solar system processes. *The Astrophysical Journal Letters*, 714(2):L217, 2010.

Nicholas Moskovitz and Eric Gaidos. Differentiation of planetesimals and the thermal consequences of melt migration. *Meteoritics & Planetary Science*, 46(6):903–918, 2011.

E Mullane, O Alard, M Gounelle, and S.S Russell. Laser ablation icp-ms study of iiiab irons and pallasites: constraints on the behaviour of highly siderophile elements during and after planetesimal core formation. *Chemical Geology*, 208(1):5 – 28, 2004. Highly Siderophile Element Behavior in High Temperature Processes.

Yanick Ricard, Ondřej Šrámek, and Fabien Dubuffet. A multi-phase model of runaway core–mantle segregation in planetary embryos. *Earth and Planetary Science Letters*, 284(1):144–150, 2009.

DC Rubie, HJ Melosh, JE Reid, C Liebske, and KEVIN Righter. Mechanisms of metal–silicate equilibration in the terrestrial magma ocean. *Earth and Planetary Science Letters*, 205(3): 239–255, 2003.

D.C. Rubie, F. Nimmo, and H.J. Melosh. Formation of earths core. In Gerald Schubert, editor, *Treatise on Geophysics*, pages 51 – 90. Elsevier, Amsterdam, 2007.

Alan E Rubin. Formation of large metal nodules in ordinary chondrites. *Journal of Geophysical Research: Planets*, 104(E12):30799–30804, 1999.

Alan E Rubin. Smyer h-chondrite impact-melt breccia and evidence for sulfur vaporization. *Geochimica et Cosmochimica Acta*, 66(4):699–711, 2002.

AM Rubin. PROPAGATION OF MAGMA-FILLED CRACKS. *Annual Review of Earth and Planetary Sciences*, 23:287–336, 1995.

Tracy Rushmer, Nick Petford, Munir Humayun, and Andrew J Campbell. Fe-liquid segregation in deforming planetesimals: Coupling core-forming compositions with transport phenomena. *Earth and Planetary Science Letters*, 239(3):185–202, 2005.

Henri Samuel. A re-evaluation of metal diapir breakup and equilibration in terrestrial magma oceans. *Earth and Planetary Science Letters*, 313:105–114, 2012.

Hiroki Senshu, Kiyoshi Kuramoto, and Takafumi Matsui. Thermal evolution of a growing mars. *Journal of Geophysical Research: Planets*, 107(E12), 2002.

VS Solomatov. Fluid dynamics of a terrestrial magma ocean. *Origin of the Earth and Moon*, pages 323–338, 2000.

Ondřej Šrámek, Yanick Ricard, and Fabien Dubuffet. A multiphase model of core formation. *Geophysical Journal International*, 181(1):198–220, 2010.

DJ Stevenson. Fluid dynamics of core formation. In *Topical Conference Origin of the Earth*, volume 681, page 87, 1988.

Dieter Stöffler, Klaus Keil, and E. R. D Scott. Shock metamorphism of ordinary chondrites. *Geochimica et Cosmochimica Acta*, 55(12):3845–3867, 1991.

S Tachibana, GR Huss, NT Kita, G Shimoda, and Y Morishita. 60fe in chondrites: Debris from a nearby supernova in the early solar system? *The Astrophysical Journal Letters*, 639 (2):L87, 2006.

Ralf Tappert, John Foden, and Allan Pring. The mineralogy of the yaringie hill meteoritea new h5 chondrite from south australia. *Meteoritics & planetary science*, 44(11):1687–1693, 2009.

Hidenori Terasaki, Daniel J Frost, David C Rubie, and Falko Langenhorst. Percolative core formation in planetesimals. *Earth and Planetary Science Letters*, 273(1):132–137, 2008.

Andrew G Tomkins, Roberto F Weinberg, Bruce F Schaefer, and Andrew Langendam. Disequilibrium melting and melt migration driven by impacts: Implications for rapid planetesimal core formation. *Geochimica et Cosmochimica Acta*, 100:41–59, 2013.

W Brian Tonks and H Jay Melosh. Core formation by giant impacts. *Icarus*, 100(2):326–346, 1992.

Harold C Urey. The cosmic abundances of potassium, uranium, and thorium and the heat balances of the earth, the moon, and mars. *Proceedings of the National Academy of Sciences*, 41(3):127–144, 1955.

NP Walte, JK Becker, PD Bons, DC Rubie, and DJ Frost. Liquid-distribution and attainment of textural equilibrium in a partially-molten crystalline system with a high-dihedral-angle liquid phase. *Earth and Planetary Science Letters*, 262(3):517–532, 2007.

Michael J Walter and Reidar G Trønnes. Early earth differentiation. *Earth and Planetary Science Letters*, 225(3):253–269, 2004.

Paul H. Warren, Finn Ulff-Mller, Heinz Huber, and Gregory W. Kallemeyn. Siderophile geochemistry of ureilites: A record of early stages of planetesimal core formation. *Geochimica et Cosmochimica Acta*, 70(8):2104 – 2126, 2006.

George W Wetherill. Formation of the earth. *Annual Review of Earth and Planetary Sciences*, 18(1):205–256, 1990.

Elisabeth Widom, Alan E Rubin, and John T Wasson. Composition and formation of metal nodules and veins in ordinary chondrites. *Geochimica et Cosmochimica Acta*, 50(9):1989–1995, 1986.

F Wlotzka. A weathering scale for the ordinary chondrites. *Meteoritics*, 28, 1993.

Takashi Yoshino, Michael J Walter, and Tomoo Katsura. Core formation in planetesimals triggered by permeable flow. *Nature*, 422(6928):154, 2003.

Karen Ziegler, Edward D Young, Edwin A Schauble, and John T Wasson. Metal–silicate silicon isotope fractionation in enstatite meteorites and constraints on earth's core formation. *Earth and Planetary Science Letters*, 295(3):487–496, 2010.

Appendix

Table 1: Individual Yaringie Vein kamacite analyses reported in ppm part 1. Negative numbers indicate analysis was below detection level

Individual Yaringie Vein Kamacite Trace Element Analyses									
	YHT1-1	YHT1-2	YHT1-3	YHT1-4	YHT1-5	YHT1-6	YHT1-7	YHT1-8	YHT1-9
Si	977.59	-903.57	-917.34	-234.29	-268.59	313.45	708.09	-256.71	296.24
P	-97.9	-92.63	117.16	-25.15	-27.99	-25.27	101.07	-26.8	43.36
S	-13866.62	-7470.48	-5370.24	921.91	-858.87	1338.1	-591.05	-558.69	-521.15
V	-0.71	-0.75	-0.78	-0.155	-0.2	0.17	0.89	-0.21	0.37
Cr	-12	-11.2	-11.62	3.7	-3.47	4.61	15.18	-3.29	4.7
Mn	-2.54	-2.39	4.57	1.07	0.77	2.63	2.92	0.9	-0.72
Co	4742.09	4804.18	4762.86	5226.39	5133.49	5115.5	5212.05	5221.47	5225.64
Cu	103.33	125.99	118.88	79.53	97.31	90.77	79.27	76.44	73.62
As	10.82	7.47	17.25	10.93	8.34	10.39	10.23	9.75	9.22
Se	-8.3	-7.15	-7.77	-1.92	-2.34	-2.12	3.5	-2.48	-2.56
Nb	-0.41	-0.41	-0.59	-0.13	-0.18	0.16	-0.18	-0.13	-0.18
Mo	6.23	13.11	-8.42	14.36	7.87	12.12	6.74	14.72	16.41
Ru	-0.47	-0.51	-0.47	0.88	0.51	0.7	0.65	0.9	-0.22
Rh	0.093	0.208	-0.09	0.218	0.186	0.135	0.145	0.173	0.245
Ag	-0.21	0.17	0.32	0.132	0.102	0.069	-0.044	-0.047	-0.06
Pd	1.39	0.6	1.25	2.41	2.37	2	3.14	2.71	2.38
Sn	19.97	29.67	26.01	4.16	2.39	1.8	2.23	1.86	2.31
Sb	-0.97	-0.86	1.02	-0.21	-0.24	0.39	0.36	-0.23	0.73
Te	-1.63	2.08	-1.53	-0.4	-0.46	-0.36	-0.48	-0.47	-0.43
Os	-0.32	-0.17	-0.3	0.091	0.26	0.127	0.087	0.124	0.089
Ir	-0.123	-0.171	-0.13	0.145	0.198	0.101	0.117	-0.036	0.091
Pt	-0.54	0.33	0.49	0.6	0.52	0.59	0.31	0.35	0.55
Au	0.71	0.55	0.41	0.603	0.62	0.44	0.8	0.597	0.684
Pb	0.29	0.51	0.64	0.338	0.099	-0.055	0.067	-0.061	0.144

TABLE 2: Individual Yaringie vein kamacite analyses reported in ppm part 2. Negative numbers indicate analysis was below detection level

Individual Yaringie Vein Kamacite Trace Element Analyses								
	YHT1-10	YHT1-11	YHT1-12	YHT1-13	YHT4-1	YHT4-2	YHT4-3	YHT4-4
Si	-280.92	413.94	375.22	7971.27	243.83	-172.75	235.13	422.99
P	43.21	38.05	78.26	139.98	49.37	-18.27	33.99	18.98
S	1129.73	-471.49	790.77	-371.28	669.86	433.02	248.05	252.69
V	-0.21	-0.22	0.19	1.31	-0.107	-0.122	-0.08	-0.1
Cr	3.67	-3.65	-3.61	6.17	4.42	-2.06	3.07	5.62
Mn	1.13	-0.8	2.17	179.84	1.25	21.26	1.16	1.02
Co	5236.02	5268.61	5222.34	5117.63	5228.57	5257.32	5207.03	5204.74
Cu	74.59	80.64	86.35	82.92	91.27	80.25	92.8	97.43
As	12.19	13.38	8.63	10.96	9.22	11.47	9.13	12.5
Se	-1.9	-2.66	-2.64	-2.56	-1.38	1.67	-1.52	-1.17
Nb	-0.19	-0.2	-0.15	0.37	-0.07	-0.085	-0.091	-0.11
Mo	5.04	7.29	10.12	7.74	18.41	13.96	15.15	10.16
Ru	0.62	0.5	0.57	0.58	0.68	0.75	0.42	0.61
Rh	0.174	0.086	0.155	0.138	0.149	0.254	0.175	0.092
Ag	-0.057	-0.06	-0.055	-0.057	-0.021	-0.026	-0.031	-0.03
Pd	2.75	2.81	2.19	2.55	2.08	2.66	2.28	2.63
Sn	2.05	1.82	-0.56	2.34	2.11	3.21	2.54	2.23
Sb	-0.27	-0.27	0.31	-0.24	0.36	0.34	-0.162	0.21
Te	0.52	-0.48	0.71	-0.52	-0.23	-0.28	-0.34	0.34
Os	-0.09	0.128	-0.093	-0.075	0.206	0.42	0.29	0.25
Ir	0.054	0.099	-0.051	0.078	0.216	0.222	0.127	0.237
Pt	0.43	0.74	0.92	0.38	0.78	0.77	0.77	0.77
Au	0.622	0.677	0.552	0.59	0.597	0.584	0.7	0.736
Pb	0.093	0.1	-0.081	0.198	-0.039	-0.039	-0.039	0.098

Table 3: Individual Yaringie matrix kamacite analyses reported in ppm. Negative numbers indicate analysis was below detection level

Individual Yaringie Matrix Kamacite Analyses							
	YHT4-met-mat-1	YHT4-met-mat-2	YHT4-met-mat-3	YHT4-met-mat-4	YHT4-met-mat-5	YHT4-met-mat-6	YHT4-met-mat-7
Si	852.68	512.54	425.8	256.08	-197.91	205.49	8058.52
P	33.77	-17.32	29.14	30.82	-19.27	37.73	-16.44
S	868.51	103.33	131.21	-67.69	-69.72	-62.88	-57.12
V	0.163	-0.11	-0.111	-0.122	-0.11	0.122	1.72
Cr	5.39	5.66	-2.08	3.9	-2.24	2.52	22.1
Mn	9.84	1.81	1.72	2.22	0.76	2.5	136.8
Co	4993.17	4974.52	4740.3	4689.22	4772.68	4905.04	4951.98
Cu	73.96	76.62	93.51	84.13	83.42	79.68	79.61
As	12.04	11.32	9.45	9.12	11.12	13.65	12.96
Se	3.65	-1.4	-1.28	-1.38	-1.88	-1.41	-1.16
Nb	-0.065	-0.064	0.08	-0.056	-0.1	0.05	-0.046
Mo	13.6	8.96	10.06	9.3	7.04	9.81	8.28
Ru	2.04	1.39	1.49	1.37	0.99	0.49	0.46
Rh	0.69	0.63	0.56	0.493	0.433	0.231	0.148
Ag	-0.024	-0.029	-0.033	-0.034	0.047	0.032	-0.028
Pd	3.03	3.34	3	2.75	3.01	2.72	2.41
Sn	5.15	1.79	1.68	1.78	1.23	1.97	5.9
Sb	0.34	-0.153	0.15	18.04	-0.156	-0.143	0.52
Te	0.79	-0.28	-0.28	0.28	0.34	-0.23	-0.26
Os	1.17	0.43	0.37	0.45	0.67	0.059	0.111
Ir	1.06	0.51	0.39	0.47	0.47	0.124	0.055
Pt	3.66	2.01	1.55	1.83	1.81	0.9	0.62
Au	0.613	0.81	0.612	0.698	0.584	0.635	0.668
Pb	0.067	-0.04	-0.042	-0.037	0.068	-0.044	0.279

TABLE 4: Individual Yaringie vein troilite analyses reported in ppm. Negative numbers indicate analysis was below detection level

Individual Yaringie Vein Troilite Trace Element Analyses						
	YHT4-sulf1	YHT4-sulf1Big	YHT4-sulph2big	YHT4-sulph3big	YHT4-sulph4big	YHT5-sulph5big
Si	1516.74	2457.09	1831.31	1464.18	1297.71	2104.62
P	190.88	245.84	190.05	168.33	166.69	170.94
S	340230.56	340230.53	340230.56	340230.56	340230.56	340230.56
V	1437.25	1561.7	1313.48	1053.46	1506.95	1067.22
Cr	599.27	722.06	1224.7	1315.04	533.79	375.37
Mn	203.45	267.35	270.64	184.42	1205.74	487.53
Co	248.02	3307.58	2116.74	83.48	111.53	780.49
Cu	3571.97	6987.26	5470.51	3352.55	2727.56	2128.93
As	-0.124	0.91	0.55	0.118	0.215	0.239
Se	124.61	122.93	126.43	119.55	127.98	119.47
Nb	3.43	7.77	3.49	3.38	1.96	2.65
Mo	996.76	1189.25	946.19	1112.05	1778.56	746.96
Ru	-0.024	0.035	0.0236	0.0066	-0.0044	0.0131
Rh	-0.0035	0.0141	0.0078	0.0028	0.0043	0.0022
Ag	0.24	0.333	0.067	0.063	0.399	0.217
Pd	0.024	0.088	0.054	0.0088	0.0119	0.027
Sn	2130.13	15080.41	605.5	47.98	873.99	9545.07
Sb	29.29	392.85	20.82	0.97	11.8	223.83
Te	0.055	0.058	0.074	0.158	0.117	0.056
Os	-0.0093	0.035	0.0111	-0.0022	0.0022	0.0099
Ir	-0.0044	0.0181	0.0025	-0.00212	-0.0017	-0.0022
Pt	-0.0125	0.049	0.028	-0.0061	-0.0062	0.0089
Au	-0.0046	0.0319	0.0146	0.0022	-0.00113	0.0041
Pb	0.116	0.727	0.0599	0.0153	0.097	0.783

Table 5: Individual Yaringie matrix troilite analyses reported in ppm. Negative numbers indicate analysis was below detection level

Individual Yaringie Matrix Troilite Trace Element Analyses						
	YHT4-sulph-mat-1	YHT4-sulph-mat-2	YHT4-sulph-mat-3	YHT5-sulph-mat-1	YHT5-sulph-mat-2	YHT5-sulph-mat-3
Si	1236.14	50363.21	9021.02	186828.63	48969.64	14592.33
P	164.2	570.53	154.04	6497.51	386.23	309.17
S	340230.56	340230.56	340230.56	340230.56	340230.56	333559.38
V	527.81	721.57	361.29	1736.14	418.09	317.6
Cr	120.44	919.35	172.32	3356.62	307.6	168.04
Mn	203.67	1134.53	305.8	3509.24	1504.83	345.56
Co	2124.5	381.47	82.38	93.34	84.16	67.47
Cu	1272.56	4054.11	972.15	1034.48	2358	724.46
As	0.84	0.74	0.147	0.29	0.137	0.125
Se	130.22	124.17	123.13	125.82	124.47	120.37
Nb	1.97	13.92	8.84	30.88	6.47	7.28
Mo	466.69	223.36	306.85	660.15	323.93	381.37
Ru	0.102	1.05	0.044	0.125	0.044	0.022
Rh	0.0231	0.18	-0.00115	0.0106	0.009	-0.00082
Ag	0.393	0.105	0.0337	0.129	0.0351	0.0198
Pd	0.104	0.358	-0.006	0.097	-0.004	-0.0056
Sn	137.13	641.66	37.96	1140.4	3.66	264.52
Sb	7.62	13.88	0.65	80.3	0.59	16.94
Te	-0.024	0.037	0.027	0.058	0.028	0.016
Os	0.094	2.22	0.0047	0.47	0.0108	-0.0027
Ir	0.067	1.33	-0.00196	0.46	0.0021	0.00113
Pt	0.139	2.57	0.0084	0.269	0.006	-0.0057
Au	0.031	0.092	-0.00142	0.046	-0.00137	-0.00124
Pb	0.0363	0.108	0.0297	0.159	0.0272	0.0591

TABLE 6: Individual Disko Island iron analyses reported in ppm. Negative numbers indicate analysis was below detection level

Individual Disko Island Iron Trace Element Analyses										
	MET-1	MET-2	MET-3	MET-4	MET-5	MET-6	MET-7	MET-8	MET-9	MET-10
Si	231.84	233.89	125.27	201.72	187.1	160.45	154.66	171.72	105.79	115.99
P	362.1	508.09	479.93	476.79	478.29	398.73	533.14	415.97	398.54	390.14
S	165.36	127.27	109.25	134.42	124.72	142.78	115.91	118.5	115.07	207.52
V	1.781	3.49	3.3	3.79	3.84	0.833	0.684	0.329	0.0954	0.898
Cr	36.49	51.56	45.3	47.88	48.63	29.2	24.71	13.51	5.07	19.69
Mn	2.73	2.3	2.08	2.12	2.13	2.16	2.31	1.87	1.78	1.8
Co	6999.98	6336.23	6074.78	6000.07	6069.99	6577.86	7092.84	6652.67	6993.53	5948.17
Cu	1412.31	1377.94	1332.13	1315.45	1338.05	1260.26	1332.45	1141.92	1020.77	1013.84
As	295.36	243.85	212.02	208.94	211.49	252.55	281.83	244.85	271.19	191.73
Se	-0.24	0.32	-0.147	-0.15	0.236	-0.168	0.343	-0.135	0.243	0.106
Nb	-0.00133	0.00221	0.00049	-0.00057	0.00263	0.00095	0.00219	0.00188	0.00171	0.00064
Mo	90.83	73.62	72.16	73	55.38	80.99	85.48	81.99	91.76	72.32
Ru	-0.036	0.092	0.081	0.11	0.097	0.063	0.088	0.107	0.148	0.181
Rh	0.0556	0.0464	0.0512	0.0544	0.0597	0.0548	0.0549	0.0445	0.0506	0.0492
Ag	0.0195	0.0206	0.0191	0.033	0.0313	0.0117	0.0241	0.0139	0.0071	0.0173
Pd	0.113	0.148	0.1121	0.126	0.135	0.13	0.123	0.123	0.156	0.1169
Sn	13.73	10.44	8.7	8.86	9.25	12.02	13.47	11.59	12.52	8.64
Sb	4.14	3.22	2.67	2.72	2.87	3.61	4.02	3.66	3.79	2.68
Te	-0.043	-0.038	0.033	-0.037	-0.042	-0.042	0.043	-0.04	-0.03	-0.022
Os	0.0283	0.0193	0.0056	0.0257	0.0312	0.0471	0.0356	0.0491	0.074	0.141
Ir	0.0091	0.0138	0.0073	0.0097	0.0257	0.0319	0.0262	0.0276	0.0502	0.131
Pt	0.323	0.234	0.222	0.337	0.382	0.358	0.332	0.543	0.578	1.004
Au	0.082	0.077	0.0807	0.0785	0.0878	0.0721	0.125	0.1113	0.1159	0.0926
Pb	0.041	0.0218	0.0256	0.0321	0.0361	-0.0119	0.0392	0.0265	0.0209	0.255

Table 7: Individual Disko Island troilite analyses reported in ppm. Negative numbers indicate analysis was below detection level

Individual Disko Island Troilite Trace Element Analyses										
	SULF-1	SULF-2	SULF-3	SULF-4	SULF-5	SULF-6	SULF-7	SULF-8	SULF-9	SULF-10
Si	21710.07	66044.25	8654.41	7304.05	13276.93	6850.79	61989.19	46211.25	36933.99	1977.14
P	437.14	993.08	975.18	166.92	279663.22	184.07	1163.32	786.01	684.57	92.25
S	350237.34	350237.31	350237.34	350237.31	350237.34	350237.38	350237.38	350237.38	350237.38	350237.38
V	555.93	243.13	309.96	806.7	451.25	774.8	442.32	356.75	545.72	893.63
Cr	386.54	162.45	406.01	849	416.27	712.31	266.04	217.2	285.89	832.06
Mn	3453.25	3040.89	3432.39	3227.65	5294.84	2981.62	2650.93	2077.89	2011.21	2869.06
Co	5980.67	6160.39	10082.88	5021.14	5770.97	4528.63	28353.95	20143.59	21768.96	4202.86
Cu	66440.9	65095.19	35402.29	35842.21	31640.26	20270.66	37350.97	79709.41	34142.61	21362.77
As	1.94	2.74	12.45	1.033	2.6	1.678	81.94	56.82	62.82	1.397
Se	35.15	45.17	80.95	31.42	38.21	36.09	38.32	55.26	37.37	28.79
Nb	0.224	0.37	1.57	0.494	0.82	0.194	-0.078	0.15	0.242	0.469
Mo	1747.21	1919.92	1195.08	1784.66	1526.34	2005.13	6801.38	2481.49	2796.57	1192.71
Ru	0.0085	0.0124	0.0164	0.0026	0.015	0.0045	0.091	0.0478	0.0287	0.0044
Rh	0.488	0.461	0.253	0.264	0.234	0.1514	0.275	0.622	0.264	0.1617
Ag	18.38	19.17	3.25	0.872	1.803	0.632	1.029	5.12	0.657	0.294
Pd	0.0342	0.0128	0.0377	0.007	0.0228	0.0039	0.083	0.0745	0.0501	0.0023
Sn	1.4	4.04	8.64	1.17	7.55	0.81	36.41	27.11	21.62	1.07
Sb	0.465	0.444	1.75	0.14	0.71	0.142	8.76	6.59	6.66	0.184
Te	1.282	3.12	2.74	0.377	1.315	0.246	0.78	1.017	0.517	0.23
Os	0.00218	0.00111	0.0037	-0.00088	-0.0005	-0.00064	0.0061	-0.0015	-0.00157	-0.00082
Ir	-0.00112	-0.00096	0.0026	-0.00056	-0.00066	-0.00075	0.0077	0.0041	-0.0013	-0.00062
Pt	-0.0034	-0.003	0.0179	0.0028	-0.00143	-0.0025	0.126	0.0386	0.033	-0.0019
Au	0.004	0.003	0.0125	0.0017	0.0283	-0.001	0.0452	0.0343	0.0324	0.0035
Pb	11633.13	1075.88	4542.53	21.98	296.5	20.45	63.94	452.55	217.23	14.45